Article

SOURCE DATA | TRANSPARENT PROCESS | OPEN ACCESS

EMBO reports

DOT1L activity affects neural stem cell division mode and reduces differentiation and ASNS expression

Bismark Appiah[1,2,†,‡], Camila L Fullio[1,2,†], Chiara Ossola[3], Ilaria Bertani[3], Elena Restelli[3], Arquimedes Cheffer[1], Martina Polenghi[3], Christiane Haffner[4], Marta Garcia-Miralles[1], Patrice Zeis[2,5,6], Martin Treppner[2,7,8], Patrick Bovio[1,2], Laura Schlichtholz[9], Aina Mas-Sanchez[9,10], Lea Zografidou[9], Jennifer Winter[9,11], Harald Binder[7,8], Dominic Grün[12,13], Nereo Kalebic[3], Elena Taverna[3,*] & Tanja Vogel[1,14,15,**]

Abstract

Cortical neurogenesis depends on the balance between self-renewal and differentiation of apical progenitors (APs). Here, we study the epigenetic control of AP's division mode by focusing on the enzymatic activity of the histone methyltransferase DOT1L. Combining lineage tracing with single-cell RNA sequencing of clonally related cells, we show at the cellular level that DOT1L inhibition increases neurogenesis driven by a shift of APs from asymmetric self-renewing to symmetric neurogenic consumptive divisions. At the molecular level, DOT1L activity prevents AP differentiation by promoting transcription of metabolic genes. Mechanistically, DOT1L inhibition reduces activity of an EZH2/PRC2 pathway, converging on increased expression of asparagine synthetase (ASNS), a microcephaly associated gene. Overexpression of ASNS in APs phenocopies DOT1L inhibition, and also increases neuronal differentiation of APs. Our data suggest that DOT1L activity/PRC2 crosstalk controls AP lineage progression by regulating asparagine metabolism.

Keywords asparagine synthetase; DOT1L; epigenetics; fate choice; metabolic regulation

Subject Categories Development; Neuroscience; Stem Cells & Regenerative Medicine

DOI 10.15252/embr.202256233 | Received 5 October 2022 | Revised 26 May 2023 | Accepted 5 June 2023

EMBO Reports (2023) e56233

Introduction

The six-layered cerebral cortex has been studied extensively with regard to the transcription factors (TFs) governing the determination of cell identity of stem and progenitor cells, as well as the generation of neurons during embryonic development and in neurodevelopmental disorders (NDD) (Molyneaux *et al*, 2007; Arnold *et al*, 2008; Britanova *et al*, 2008; Bedogni *et al*, 2010; Clark *et al*, 2020). Neural stem and progenitor cells are classified into two main types based on the location of mitosis: apical progenitors (APs) that divide at the apical surface of the ventricular zone, and basal progenitors (BPs) that typically divide in the subventricular zone (SVZ) (Taverna *et al*, 2014). In rodents, APs and BPs differ not only in localisation but also in their mode of division and neurogenic potential. At

1 Institute of Anatomy and Cell Biology, Department of Molecular Embryology, Faculty of Medicine, Albert-Ludwigs-University Freiburg, Freiburg, Germany
2 Faculty of Biology, Albert-Ludwigs-University Freiburg, Freiburg, Germany
3 Human Technopole, Milan, Italy
4 Max Planck Institute for Molecular Cell Biology and Genetics, Dresden, Germany
5 Max Planck Institute of Immunobiology and Epigenetics, Freiburg, Germany
6 International Max Planck Research School for Molecular and Cellular Biology (IMPRS-MCB), Freiburg, Germany
7 Institute of Medical Biometry and Statistics, Faculty of Medicine and Medical Center, Albert-Ludwigs-University Freiburg, Freiburg, Germany
8 Freiburg Center for Data Analysis and Modeling, Albert-Ludwigs-University Freiburg, Freiburg, Germany
9 Institute for Human Genetics, University Medical Center of the Johannes Gutenberg University Mainz, Mainz, Germany
10 Institute of Molecular Biology (IMB) gGmbH, Mainz, Germany
11 German Resilience Centre, University Medical Center Mainz, Mainz, Germany
12 Würzburg Institute of Systems Immunology, Max Planck Research Group at Julius-Maximilians-University Würzburg, Würzburg, Germany
13 Helmholtz Institute for RNA-based Infection Research (HIRI), Helmholtz-Center for Infection Research (HZI), Würzburg, Germany
14 Center for Basics in NeuroModulation (NeuroModul Basics), Medical Faculty, Albert-Ludwigs-University Freiburg, Freiburg, Germany
15 Freiburg Institute for Advanced Studies (FRIAS), Albert-Ludwigs-University Freiburg, Freiburg, Germany
*Corresponding author. Tel: +39 3472190463; E-mail: elena.taverna@fht.org
**Corresponding author. Tel: +49 761 2035086; E-mail: tanja.vogel@anat.uni-freiburg.de
†These authors contributed equally to this work as first authors
‡Present address: Institute of Medical Bioinformatics and Systems Medicine, Medical Center–University of Freiburg, Faculty of Medicine, University of Freiburg, Freiburg, Germany

mid-neurogenesis mouse APs mainly undergo asymmetric, self-renewing division to generate one AP and one BP. In contrast, mouse BPs are mainly undergoing symmetric neurogenic consumptive division to generate two neurons (Taverna *et al*, 2014).

The relevance of maintaining a tight balance between different modes of divisions is illustrated by primary microcephaly (Fish *et al*, 2006), a human NDD, where the premature switch to neurogenic consumptive division was identified as a key driver of the dramatic reduction in brain size observed in patients. Recent work has identified TF activities, mitotic spindle components (Haydar *et al*, 2003) and specific metabolic signatures (Lange *et al*, 2016; Zheng *et al*, 2016; Journiac *et al*, 2020) as potential molecular regulators of the AP division mode. Among TFs, master regulators of AP identity such as SOX2, PAX6 and EMX2 were reported to promote the symmetric divisions of APs (Heins *et al*, 2001; Estivill-Torrus *et al*, 2002; Asami *et al*, 2011; Hagey & Muhr, 2014).

But despite the progress in the definition of the genetic logic of cell fate determination and acquisition of cell identity (Molyneaux *et al*, 2007), little is still known about the epigenetic regulation of the division mode, an aspect that is crucially linked to the symmetry and asymmetry of cell fate specification in APs. Defining the relationship between epigenetics and symmetry/asymmetry of division is important considering that (i) epigenetic information is heritable and can affect cell fate decision (Hirabayashi & Gotoh, 2010), and (ii) histone proteins can be asymmetrically partitioned during cell division (Wooten *et al*, 2020; Roubinet *et al*, 2021). These data demand for extending the sparse insights as of yet into the cellular and mechanistic link between epigenetic regulation and NDDs (Bjornsson, 2015; Mastrototaro *et al*, 2017).

We recently reported that the chromatin-modifier disruptor of telomeric silencing-like 1 (DOT1L) affects cortical development. Genetic inactivation of DOT1L at early stages of neurogenesis (around E9.5 in mice) depleted the progenitor pool and resulted in premature differentiation to neurons (Franz *et al*, 2019). Moreover, pharmacological inhibition of DOT1L in cultured mouse neural progenitor cells (NPCs) led to increased neuronal differentiation, which correlated with DOT1L-mediated alteration of accessibility of SOX2-bound enhancer regions (Ferrari *et al*, 2020). Interestingly, DOT1L is linked to genes known to regulate the symmetry and asymmetry of cell division and cell metabolism in neural stem and progenitor cells (Roidl *et al*, 2016; Franz *et al*, 2019). These observations prompted us to study how DOT1L affects specifically AP behaviour and lineage progression in the cerebral cortex *in vivo* during mid-neurogenesis (around E14.5 in mice).

By using single-cell labelling and two lineage tracing techniques, in combination with single-cell RNA sequencing (scRNA-seq) and cell biological enquiry, we show that DOT1L affects the division mode and the choice between self-renewal and differentiation of APs during cortical development. Mechanistically, our data show that DOT1L activity maintains AP self-renewal potential by hampering the premature activation of metabolic programmes of differentiated cells and by preventing dissipation of the poised promoter state and conserving PRC2-mediated H3K27me3 silencing.

Results

DOT1L inhibition increases delamination

DOT1L is expressed in cortical progenitors and neurons throughout early- (E12.5), mid- (E14.5) and late- (E16.5) neurogenesis (Fig EV1A) (Franz *et al*, 2019). Previous data, using either genetic ablation *in vivo* (Franz *et al*, 2019) or pharmacological inhibition of DOT1L *in vitro* (Roidl *et al*, 2016; Ferrari *et al*, 2020), suggest that DOT1L controls the generation of neurons. However, information is lacking on (i) whether DOT1L exerts its function by its scaffolding or enzymatic activity *in vivo*, and (ii) which molecular mechanisms are in place. To fill this gap in knowledge, we here specifically focus on DOT1L's enzymatic activity by pharmacologically perturbing DOT1L in the mouse developing brain during mid-neurogenesis. To this end, we treated mouse E14.5 hemispheres with EPZ5676 (EPZ), a widely used inhibitor of DOT1L in cancer research (Nassa *et al*, 2019; Vlaming *et al*, 2019; Vatapalli *et al*, 2020) and during reprogramming (Cao *et al*, 2018). After 24 h in brain hemisphere rotation (HeRo) culture (Schenk *et al*, 2009) (Appendix Fig S1), EPZ reduced H3K79me2 levels (Fig EV1B). To understand the consequences of H3K79me2 levels reduction for neurogenesis, we took advantage of the fact that in the rodent neocortex, the acquisition of a basal fate (BP or neuron) is concomitant with the relocation of the centrosome and associated cilia from the ventricular surface to an abventricular location (Fish *et al*, 2006; Tavano *et al*, 2018). Using immunofluorescence for organelle-specific markers, we assessed the number and distribution of centrosomes (as revealed by TUBG1

Figure 1. Basal localisation of centrosomes and cilia in the VZ indicates delamination of progenitors upon DOT1L inhibition.

A Overview of immunofluorescence staining for centrosomes (TUBG1) and cilia (ARL13B) in control (Con) (left) and EPZ-treated sections (right). Dotted lines mark either ventricular (bottom part) or pial (top part) surface of the tissue.

B Left: quantification of total centrosome numbers in control and EPZ-treated sections in 100 μm. Right: number of centrosomes in ventricular zone (VZ), subventricular zone (SVZ) and cortical plate (CP) expressed as percentage of total per condition.

C Left: quantification of total cilia numbers in control and EPZ-treated sections in 100 μm. Right: number of cilia in VZ, SVZ and CP expressed as percentage of total per condition.

D Overview of VZ showing TUBG1 and ARL13B immunofluorescence staining in control (top) and EPZ (bottom) condition. Squared parentheses indicate the ventricular and abventricular compartments. Dotted lines mark ventricular surface of tissue slide.

E, F (E) Quantification of TUBG1- and (F) ARL13B-positive structures in ventricular and abventricular compartments expressed as percentage of the total number per condition.

Data information: All distributions of TUBG1 and ARL13B are based on quantifications of four fields of view including the relevant area to quantify (VZ, SVZ, and CP), from four independent experiments ($n = 4$; for the distribution in the cortical wall: Con: 755 ARL13B-positive structures and 1,123 TUBG1-positive structures; EPZ: 715 ARL13B-positive structures and 1,123 TUBG1-positive structures; for the distribution in the VZ, Con: 633 ARL13B-positive structures and 1,005 TUBG1-positive structures; EPZ: 686 ARL13B-positive structures and 1,023 TUBG1-positive structures). *T*-test, two-tails was performed for all quantifications, $*P < 0.05$, $***P < 0.001$, error bars represent SD. Scale bars in all panels: 10 μm.
Source data are available online for this figure.

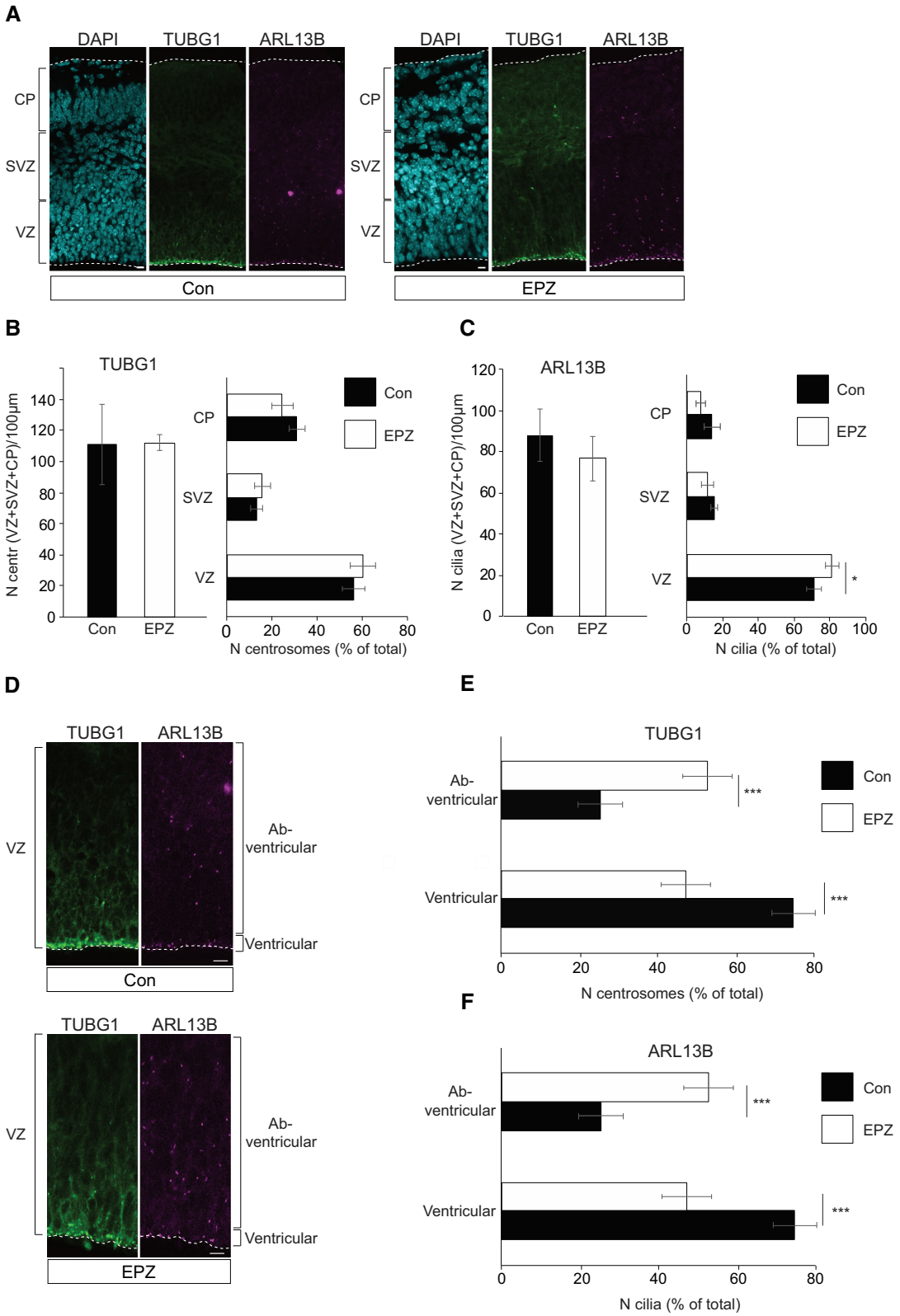

Figure 1.

staining, Fig 1A) and primary cilia (as revealed by ARL13B staining, Fig 1A) in the cortical wall as a relevant proxy for delamination (Taverna *et al*, 2012; Wilsch-Brauninger *et al*, 2012; Tavano *et al*, 2018). When assessing the entire cortical wall, these parameters were not affected quantitatively upon EPZ treatment (Fig 1B and C). However, when scoring the distribution of TUBG1- and ARL13B-positive

structures specifically in the VZ, we detected a strong increase in abventricular TUBG1- and ARL13B-positive structures in EPZ-treated samples compared to control along with a parallel decrease in ventricular centrosomes and cilia (Fig 1D–F, Appendix Figs S2 and S3, Movies EV1–EV4). These data, therefore, suggest that DOT1L inhibition increases AP delamination, possibly prompting a basal cell fate.

We next used *ex utero* electroporation of a mCherry reporter and subsequent HeRo culture for 24 h in the presence or absence of EPZ to study the effect of DOT1L inhibition on cell positioning and fate (Fig EV1C). Whereas the control mCherry-positive cell bodies resided within the apical-most half of the VZ, upon EPZ treatment, mCherry-positive cell bodies localised more basally (Fig EV1D).

We studied the effect of DOT1L inhibition by labelling cycling cells at the end of 24 h HeRo culture with a 1 h EdU pulse and analysed the number of proliferating cells as well as the fate of EdU-labelled cells by assessing SOX2 and EOMES expression. We observed an overall reduced number of cycling, EdU-positive cells and equal numbers of single $SOX2^+$ or $EOMES^+$ cells. This finding suggests that the DOT1L inhibition for 24 h impaired acutely S-phase entry or progression, but that the timeframe was too short to impact overall numbers of APs or BPs. $SOX2^+/EOMES^+$ double-positive cells increased upon DOT1L inhibition compared to controls, indicating an increased transition of APs towards a differentiative fate (Fig 2A and B). According to the reduced number of actively cycling EdU^+ cells, we observed that both $SOX2^+/EdU^+$ and $EOMES^+/EdU^+$ double-positive cells decreased upon DOT1L inhibition compared to controls (Fig 2A and B), suggesting AP cell cycle exit and acquisition of a differentiative fate, possibly a shorter presence of BPs, or impaired generation of BPs. As $SOX2^+/EOMES^+$ cells increased, the latter scenario seemed less likely compared to BPs progressing with differentiation upon DOT1L inhibition. We further investigated the effect of DOT1L inhibition on cell cycle progression of cortical progenitors by assessing the number and distribution of pHH3-positive mitotic cells (M-phase) (Fig EV1E). We observed neither a difference in the number of pHH3-positive cells nor in the distribution of pHH3-positive cells between the VZ (apical localisation) and SVZ (basal localisation) (Fig EV1F). In summary, we observed that upon DOT1L inhibition, fewer APs entered S-phase and that after cell cycle progression, they adopted a more differentiating fate. Since we observed APs in S- and M-phase as well as in a subsequent differentiating BP state, we excluded a general anti-mitotic but assumed a differentiative effect of the drug. Further, the observation of similar numbers of APs in M-phase but reduced numbers in S-phase suggested a possible alteration in the mode of mitosis, similar to our observations of the genetic loss of function of DOT1L (Franz *et al*, 2019).

We further used the *Tis21(Btg2)-Gfp* mouse to characterise the potential neurogenic bias upon DOT1L inhibition. *Tis21* (*Btg2*) is a marker expressed by neurogenic APs and therefore the *Tis21(Btg2)-Gfp* mouse model allows following neurogenesis by monitoring the appearance and localisation of GFP (Fig 2C). Notably, *Tis21* is activated in cycling APs undergoing interkinetic nuclear migration, and GFP is thus detected within the entire VZ. As a neurogenic marker, *Tis21* expression is kept in the neurogenic progeny (Haubensak *et al*, 2004). Upon DOT1L inhibition, we observed an increase in the proportion of cells positive for TIS21-GFP (Fig 2D), suggesting that more cells adopted a BP and/or neuronal fate (Haubensak *et al*, 2004). Indication for an increased neurogenic fate was also observed by staining for CTIP2 as a neuronal marker, which indicated arbitrary localisation of these neurons in the VZ upon DOT1L inhibition (Fig 2E–H). We also investigated whether we observe increased neuronal differentiation upon DOT1L knockdown (KD), in a cell-autonomous fashion. The efficiency of the DOT1L KD was shown in N2a cells and in *in utero* electroporated tissue (Fig EV1G and H). We used the *in utero* electroporation paradigm and observed that upon DOT1L KD, the expression of TUBB3 and CTIP2 increased in

Figure 2. Increased neurogenesis of APs upon DOT1L inhibition.

A Immunostaining of control and EPZ-treated sections showing SOX2 and EOMES expression and EdU labelling. Scale bar: 20 μm. Dotted lines mark ventricular surface of the tissue.

B Quantification of SOX2-, EOMES- and EdU-positive cells, and co-labelled cells normalised to 100 μm of apical surface. *T*-test was performed, $*P < 0.05$, $**P < 0.01$, error bars represent SEM. Total number of independent experiments for EdU labelling: 9 ($n = 4$ control samples, $n = 5$ EPZ-treated samples). Total number of independent experiments for SOX2, EOMES and double stainings: 6 ($n = 3$ control samples, $n = 3$ EPZ-treated samples).

C Immunofluorescence staining showing overview of TIS21-GFP-positive (GFP^+) cells in VZ of control and EPZ-treated sections. Scale bars: 10 μm. Dotted lines mark ventricular surface of the tissue. Magnifications on the right show exemplarily a TIS21-GFP-positive cell (arrow), mild positive cell (arrow with dashed line) and a negative cell (arrowhead).

D Quantification of GFP-positive and GFP-negative cells in VZ for control and EPZ conditions. Chi-square test was performed, $****P < 0.0001$, error bars represent SEM. Total number of independent experiments: 6 ($n = 3$ control samples, $n = 3$ EPZ-treated samples).

E Immunofluorescence staining showing overview of CTIP2-positive cells in control and EPZ-treated sections. Scale bars: 20 μm. Dotted lines mark either ventricular or pial surface of the tissue.

F Quantification of total CTIP2-positive cells, normalised to 100 μm of apical surface. Total number of independent experiments: 6 ($n = 3$ control samples, $n = 3$ EPZ-treated samples). Error bars represent SEM.

G Immunofluorescence staining showing SOX2-, EOMES- and CTIP2-positive cells in control and EPZ-treated sections. Scale bars: 10 μm. Dotted lines mark the ventricular surface of the tissue. Magnifications on the right show exemplarily a CTIP2-positive cell (arrowhead) that is negative for SOX2 and positive for EOMES in EPZ-treated condition.

H Quantification of CTIP2-positive cells in the VZ, normalised to 100 μm of apical surface. Total number of independent experiments: 6 ($n = 3$ control samples, $n = 3$ EPZ-treated samples). *T*-test was performed, $**P < 0.01$, error bars represent SEM.

I *In utero* electroporation of cortical tissue of shRNA against DOT1L and control alongside a GFP-expressing plasmid, followed by assessment of expression of CTIP2 and TUBB3 as markers for neuronal differentiation to study cell-autonomous and non-autonomous effects. Scale bars: 20 μm. Dotted lines mark either ventricular or pial surface of tissue slide.

J Quantification of CTIP2- and TUBB3-positive cells in VZ, SVZ, IZ and CP in control and shDot1l sections. Total number of independent experiments: 6 ($n = 3$ control shRNA, $n = 3$ shDot1l). *T*-test was performed, $*P < 0.05$, error bars represent SEM.

Source data are available online for this figure.

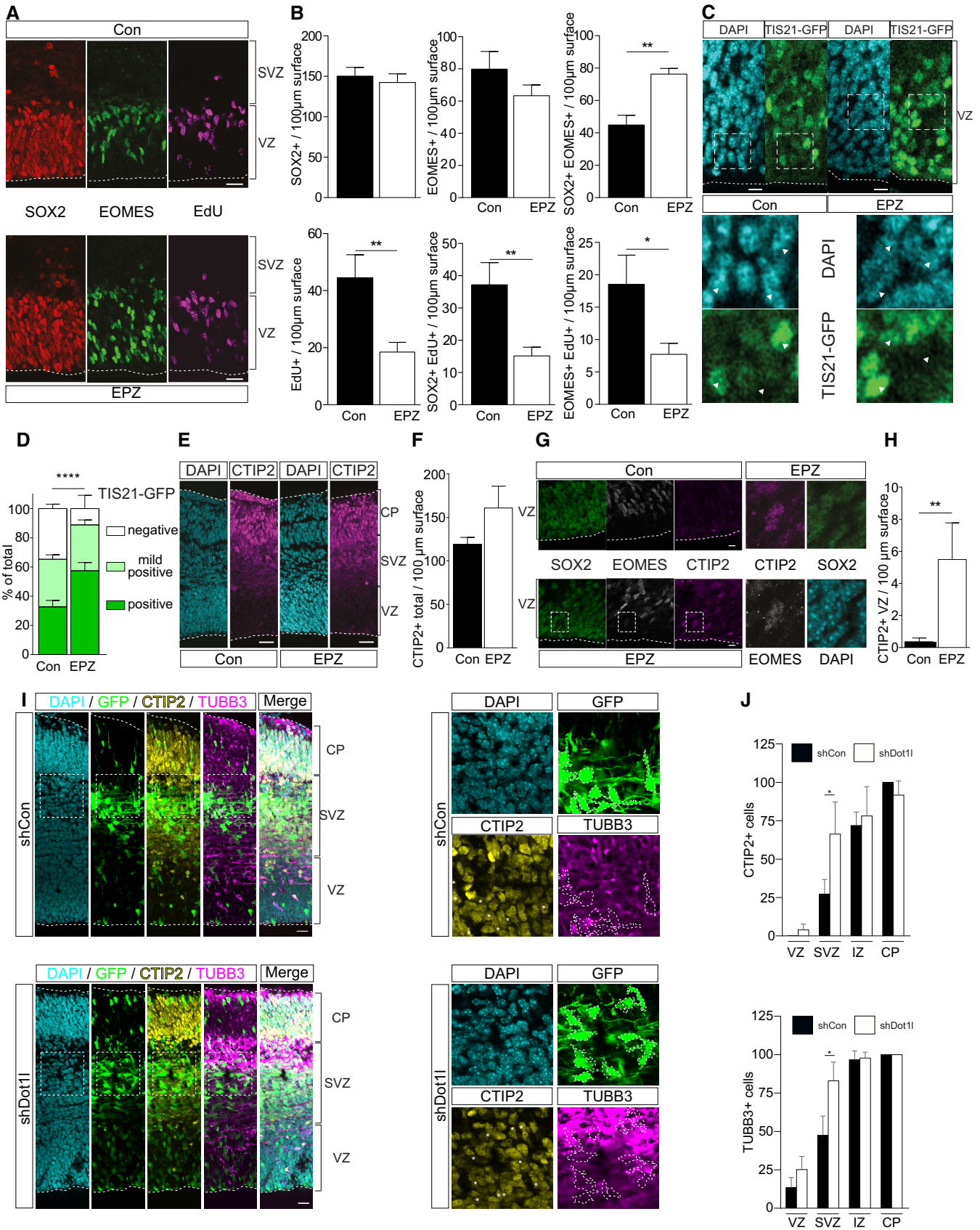

Figure 2.

GFP-positive, electroporated cells located in the VZ and SVZ (Fig 2I and J).

Our data combining cell biological enquiry, analysis of cell distribution and fate specification via marker expression suggest that upon DOT1L inhibition, the AP progeny is committed to a delaminated, more basal and differentiated fate (possibly BP/neuronal).

DOT1L inhibition promotes neuronal differentiation

To dissect the underlying cellular events at a higher temporal and spatial resolution, we used manual microinjection for targeting single APs in tissue (Taverna *et al*, 2012; Wong *et al*, 2014). APs were microinjected with Dextran-Alexa555 in organotypic slices from E14.5 wild-type mouse telencephalon (see scheme in Appendix Fig S1). The slices were kept in culture for various time windows to reconstruct and study the AP progeny. Cell identity was defined by combining several criteria, such as cell morphology, location and marker expression (Taverna *et al*, 2012; Wong *et al*, 2014; Kalebic *et al*, 2016; Tavano *et al*, 2018; Shull *et al*, 2019). Three hours after microinjection, the progeny of microinjected APs resided almost exclusively in the VZ and had contact with the ventricle (Appendix Fig S4A). Instead, 24 h after microinjection, the progeny of microinjected APs (i) located not only to the VZ but also to the SVZ and CP, and (ii) expressed the neuronal marker TUBB3 (Appendix Fig S4B, panels on the right).

Having hence successfully implemented AP microinjection, we applied it to study at the single-cell level the effect of DOT1L inhibition on cell morphology, cell identity and lineage progression (Fig 3A–F). We first quantified the progeny of microinjected cells and found that EPZ treatment did not change the proportion of cells found in two-cell clusters as opposed to single cells (Fig 3B and C). These data suggest again that EPZ did not arrest cells in the cell cycle but principally allowed cell division (Fig EV1F). The morphological analysis showed that the inhibition of DOT1L resulted in an increase in the number of cells without apical contact, lacking the typical bipolar morphology of APs (Fig 3B and D), suggesting the generation of a delaminated and more differentiated cell progeny (either BPs or neurons) compared to APs. Staining with EOMES and TUBB3 revealed no change in the fraction of EOMES-expressing cells (BPs; Fig 3B and E) compared to a strong increase in the proportion of TUBB3-expressing cells (neurons; Fig 3B and F). Taken together, these data suggest that the inhibition of DOT1L might favour APs to acquire a differentiative fate that results in the generation of increased numbers of neurons.

DOT1L inhibition promotes symmetric neurogenic division

To follow the switch to neurogenesis at single-cell resolution, microinjection into single cells was performed in the *Tis21(Btg2)-Gfp* mouse. EPZ treatment of the respective slice cultures increased the proportion of microinjected cells that are TIS21-GFP positive in the neocortex (Fig 4A and B).

To address the effects of DOT1L inhibition on the symmetry and asymmetry of AP cell division, we also made use of the high single-cell resolution provided by microinjection. Here, we analysed specifically two-daughter cell clusters and assessed their symmetry/asymmetry in terms of morphology and cell identity (Fig 4C–E). Morphological analysis revealed that EPZ treatment increased specifically the proportion of two-cell clusters where both cells delaminated (Fig 4C), suggesting that the increased delamination (shown also in Fig 3) derived from a switch to symmetric division, rather than direct delamination of APs.

The analysis of TIS21-GFP in two-daughter cell clusters revealed that upon EPZ treatment, both daughter cells expressed TIS21-GFP (Fig 4D). Moreover, in most clusters, both daughter cells expressed (symmetrically) the neuronal marker TUBB3 (Fig 4E). Taken together, these data strongly suggest that DOT1L inhibition changes the mode of division of APs from asymmetric self-renewing to symmetric neurogenic division.

DOT1L might affect fate via the reported regulation of mitotic spindle orientation and partitioning of cell biological components (Franz *et al*, 2019). We, therefore, evaluated the cleavage plane angle in mitotic APs and found no changes upon DOT1L inhibition (Fig 4F and G). Finally, we quantified the partitioning of the apical plasma membrane in mitotic AP and again found no difference upon DOT1L inhibition (Fig 4H). Taken together, these data suggest that alteration of the spindle apparatus was not a major driving force of basal fate adoption, but that other mechanism(s) might be at play. We sought to discover a new possible mechanism of action of DOT1L by using scRNA-seq on lineage-traced cells.

DOT1L inhibition alters the composition of the progenitor populations and favours neurogenesis

To gain insights into the transcriptional signature of the underlying cellular alterations upon DOT1L inhibition, we performed scRNA-seq, focusing exclusively on lineage-related cells. To this goal, we specifically labelled single APs before the start of the pharmacological treatment, using two different approaches: (i) microinjection of fluorescent dye (either Dextran-Alexa488 or Dextran-Alexa555) into single neural stem cells using a recently developed robotic microinjection system (Shull *et al*, 2019), and (ii) *ex utero* hemisphere electroporation of a GFP-expressing construct (Calegari *et al*, 2002; Schenk *et al*, 2009; Kalebic *et al*, 2019) (schemes in Appendix Fig S1). In both cases, the tissue (tissue slices for microinjection or hemispheres for *ex utero* electroporation) was kept in culture for 24 h and the labelled cells were recovered by FACS (microinjection into single neural stem cells: 307 cells (Con) and 439 cells (EPZ); *ex utero* electroporation: 371 cells (Con) and 379 cells (EPZ)). With both labelling approaches, the number and the quality of cells recovered were sufficient for subsequent scRNA-seq analysis (Appendix Fig S5A–D).

We used two different algorithms for clustering microinjected cells according to their transcriptomes. In Seurat-based clustering (Stuart *et al*, 2019), progenitors appeared as one cluster in the microinjection data set (Fig 5A), which could be separated in APs and BPs using RaceID clustering (Grun *et al*, 2015) in this data set (Fig 5B). In the electroporated cells data set, Seurat-based clustering resolved APs and BPs (Fig 5E). We plotted several known marker genes for detailed cluster annotations (for control and EPZ, and for both electroporated (Fig EV2A and B) and microinjected cells (according to RaceID clustering) (Fig EV2C and D)). This allowed us to clearly identify APs (expressing *Hes5*, *Fabp7* or *Sox2*), BPs (positive for *Neurog2*, *Eomes* or *Insm1*), different clusters of neurons (*Neurod6*, *Dcx*, *Dpysl3* or *Tubb3*), and endothelial cells (exclusively in the electroporated samples) (Fig EV2A–D).

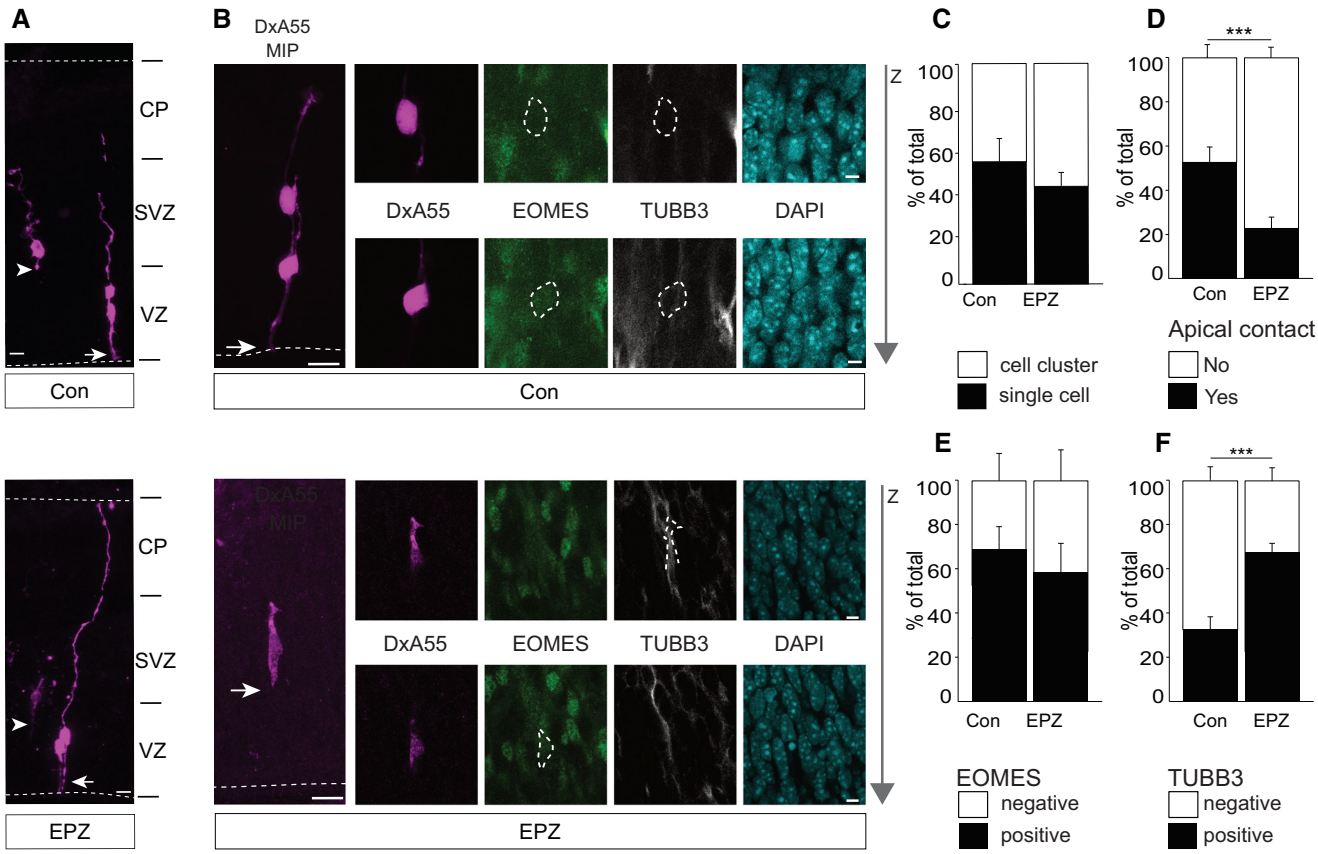

Figure 3. Lineage tracing of microinjected cortical APs shows DOT1L inhibition increases neurogenesis and apical delamination.

A Microinjected cells in the VZ (magenta) in sections treated with DMSO (Con) (upper panel) or EPZ (lower panel) showing Dx-A555-labelled cells after 24 h in slice culture. White arrow indicates the apical process contacting the ventricular surface. White arrowheads indicate the apical-directed process of delaminated cells. Scale bars: 10 μm.

B Immunofluorescence staining of microinjected sections showing the progeny of microinjected cells (a daughter cell pair) and expression of EOMES and TUBB3. White arrows indicate the apical-directed processes. Note that in the top panel, the apical-directed process contacts the ventricular surface (dotted white line) (EOMES and TUBB3 negative), while in the bottom panel, it does not contact the ventricular surface, indicating that the cell has delaminated (EOMES and TUBB3 positive). Scale bars MIP: 10 μm; insets: 5 μm.

C Quantification of microinjected cells found as single-cell or two-cell clusters, expressed as percentage of total Dx-A555-positive cells per condition.

D Quantification of microinjected cells with or without contact to the apical surface of the organotypic slice expressed as percentage of total Dx-A555-positive cells per condition. Total number of independent microinjection experiments: 6 (n = 3 wild-type embryos, n = 3 in Tis21-GFP embryos). Total number of cells scored: Con, 156 cells; EPZ, 287 cells.

E EOMES-positive and EOMES-negative cells plotted as a percentage of total cells scored per condition.

F TUBB3-positive and TUBB3-negative cells in control and EPZ conditions plotted as a percentage of total cells scored per condition.

Data information: Cell scoring based on TUBB3 or EOMES expression is from three independent experiments (n = 3; Con: 70 cells, EPZ: 113 cells). Fisher's exact test was performed for all quantifications, ***P < 0.001, error bars represent SEM. MIP—maximum intensity projection. VZ—Ventricular Zone, SVZ—Subventricular Zone, CP—Cortical Plate. Scale bars in all main panels: 20 μm, and all insets: 5 μm.
Source data are available online for this figure.

Using the Seurat-based cell clusters, we plotted the cells for each of the two conditions (control and EPZ) and showed that both conditions contributed to each cluster (Fig 5C and F). We concluded that all expected progenitor types were captured with both labelling approaches and in both conditions.

Interestingly, besides the main cell populations (APs, BPs and neurons), we identified one cell cluster lacking a known, specific transcriptional fingerprint (Fig EV2A and C). We hypothesised that our high-resolution and clonal scRNA-seq approach captured a rare transient transcriptional state that we termed TTS accordingly (Fig 5A–G). Few genes with enriched, but not unique, transcription were found in the TTS, to which belonged, for example, *Ofd1* and *Mme* (microinjection data set) as well as *Fgfr3* and *Nr2f1* (electroporation data set) (Fig EV2A–D). These genes can affect the balance between proliferation and differentiation (Mazur-Kolecka & Frackowiak, 2006; Naka *et al*, 2008; D'Angelo *et al*, 2012; Gabriel *et al*, 2016; Teratani-Ota *et al*, 2016; Huang *et al*, 2020). Furthermore, GO enrichment analysis (electroporation data set) showed that genes up-regulated in the TTS compared to APs or BPs were enriched in terms associated with apical hallmarks (Fig EV3A and B). Genes with decreased expression in the TTS cluster compared to APs or BPs were enriched in GO terms related to cell division (spindle and

centrosome organisation, midbody, kinetochore and chromatin condensation, and cyclin-dependent protein kinases) and early neuronal differentiation (distal axon) (Fig EV3A and B). Comparing the GO terms of TTS and neurons showed a decrease in genes associated with neuronal differentiation (Fig EV3C). Together, this transcriptional signature of TTS suggests that this cell state relates best to APs with reduced proliferation capacity.

While the TTS comprised a minor fraction in control conditions, its proportion increased upon EPZ treatment, together with a decrease in the proportion of APs (Fig 5D and G). We exemplarily conducted single-molecule FISH experiments using probes against *Ofd1* and *Nr2f1*, which showed an increased expression upon DOT1L inhibition compared to controls (Fig EV2E). To further characterise the TTS, we plotted the expression levels of selected cell type/state markers in APs, TTS, BPs and neurons (Fig EV4A). The best-fitting overlap was again between APs and TTS, but differences were clearly observable. The data so far suggested that TTS's transcriptional makeup described above had hallmarks of APs, but had at the same time a decreased proliferative capacity (e.g. reduced expression of Cdk-complex members (Kawauchi *et al*, 2013), including Ccna2, Cdk1, Ccnb1, Cdk6, Cks2, Cks1b, Ccnb2, Ccnd2, Pcna, Ccnd1 and Ccng2, Dataset EV1). As the number of TTS increased upon DOT1L inhibition at the expense of APs, the scRNA-seq data reflected at the transcriptional level our data on single-cell reconstruction of lineage progression and a decrease in proliferative capacity observed in the EdU pulse experiment (Fig 2B).

We next addressed whether the scRNA-seq data would also support a general increase in the differentiative fate of APs upon DOT1L

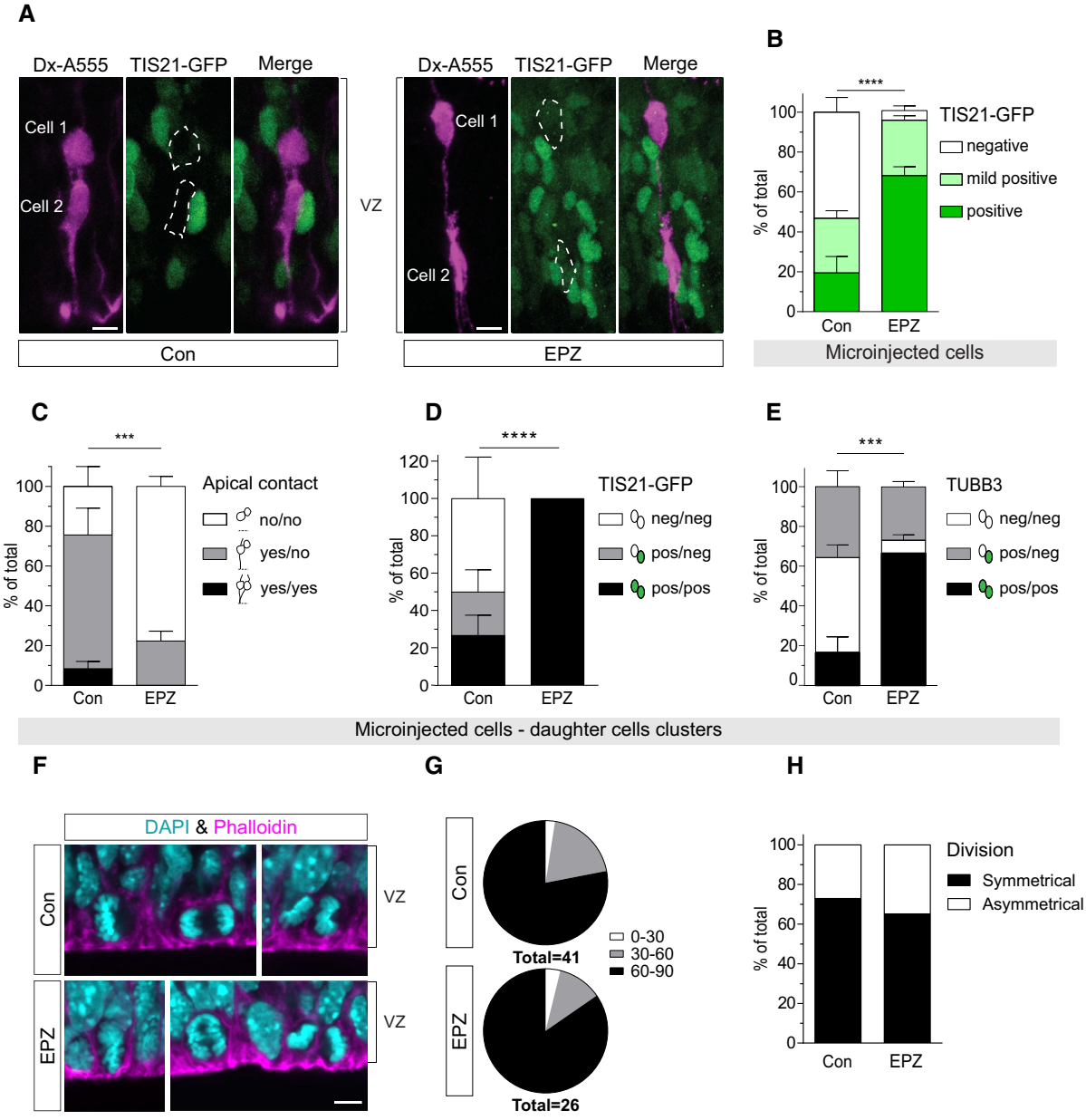

Figure 4.

Figure 4. DOT1L inhibition leads to neurogenic commitment of VZ progenitors.

A Microinjected cells in the VZ (magenta) of control (Con) and EPZ-treated slices 24 h after microinjection and slice culture. Left: daughter cell pair in control section with asymmetric GFP expression, with cell 1 (basal location) being mild GFP-positive, and cell 2 (apical location) GFP-negative. Right: EPZ-treated section showing a daughter cell pair with symmetric mild GFP-positive expression. Scale bars: 5 μm. Dotted shapes indicate the contour of Dx-A555 cell soma.

B Graph showing proportion of labelled cells expressing GFP positive, mild positive or negative, expressed as percentage of total cells per condition.

C Symmetry or asymmetry in daughter cells' apical contact (yes/yes: both cells have apical contact; yes/no: one cell has apical contact and the other not; no/no: both cells lack apical contact).

D Symmetry (pos/pos, neg/neg) or asymmetry (pos/neg) in GFP expression in daughter cells expressed as percentage of total cells per condition.

E Symmetry or asymmetry in TUBB3 expression in daughter cells plotted (pos/pos: both cells express TUBB3; pos/neg: one cell expresses TUBB3 and the other not; and neg/neg: none of the cells expresses TUBB3).

F Phalloidin staining of control and EPZ-treated sections showing cells during mitosis. Scale bar: 5 μm.

G Pie chart showing the proportion of cells with different angles of the cleavage plane in respect to the ventricular surface, divided into groups with increments of 30°.

H Percentage of cells undergoing symmetric or asymmetric cell division, defined by the cleavage plane bypassing or bisecting the apical plasma membrane, in control and EPZ-treated samples.

Data information: Quantifications shown in Fig 4B–E are based on three independent experiments (n = 3, biological replicates) and Chi-square test was performed in all cases. Error bars represent SEM, ***P < 0.001, ****P < 0.0001, alpha = 0.05. VZ—ventricular zone. The following number of cells were scored: (B) TIS21-GFP—267 total cells were quantified (Con: 86 cells, EPZ: 181 cells). (C) Apical contact—85 total daughter cell pairs (Con: 31 pairs, EPZ: 54 pairs). (D) TIS21-GFP—58 total daughter cell pairs (Con: 21 pairs, EPZ: 37 pairs). (E) TUBB3—50 total daughter cell pairs (Con: 17 pairs, EPZ: 33 pairs). (G) For control condition, 41 cells from four independent samples, five sections and 15 different images were assessed. EPZ-treated quantifications were performed on a total of 26 cells from three independent samples, five sections and 16 images. (H) For control condition, a total of 37 cells from four independent samples, five sections and 15 different images were assessed. EPZ-treated quantifications were performed on a total of 23 cells from three independent samples, five sections and 16 images.
Source data are available online for this figure.

inhibition. To this end, we aimed at inferring lineage trajectories from the electroporated scRNA-seq data. We could not use scVelo, an algorithm that predicts trajectories on the basis of the ratio of spliced and unspliced transcripts (La Manno *et al*, 2018), as in our data set the proportions between spliced/unspliced transcripts were equally distributed, and the inferred lineage trajectory was against the known biological relation, that is, neurons projecting towards progenitors (Fig EV4B). Instead, we used two cluster-based prediction tools, Slingshot (Street *et al*, 2018) and Monocle (Cao *et al*, 2019). In the control condition, both algorithms revealed that APs have a higher probability to generate the TTS, which can resolve in BPs and/or neurons (Fig EV4C and D). Upon DOT1L inhibition, Slingshot predicted that both APs and BPs differentiate towards the TTS, which gives rise to neurons, in accordance with our extensive histological marker expression analysis shown before. The lineage trajectories were less clear using Monocle, predicting the TTS followed both APs and BPs, but failed to connect the TTS directly to neurons (Fig EV4C and D). To address the question of whether the TTS expressed differentiative marker genes, we plotted the co-expression of *Eomes* and *Tubb3* in the electroporated data set, which showed that very few cells classified as TTS co-expressed both markers (Fig EV4E). Instead, the TTS cluster contained cells expressing either *Eomes* or *Tubb3* at different levels, and cells negative for both markers. This observation suggested that the TTS reflects an uncommitted cell state that may directly follow after the end of mitosis when cell-specific transcription is reinitiated (Palozola *et al*, 2017).

DOT1L inhibition favours neuronal lineage progression by PRC2 de-repression of metabolic genes

As we ruled out alterations of the cleavage angle as major driving force of differentiative divisions of APs (Fig 4F and G), we next aimed to elucidate which alternative molecular mechanism was underlying changes in neuronal lineage progression and the switch of APs towards neurogenic division upon DOT1L inhibition. We performed unbiased analysis of (i) alterations of TF activities in gene regulatory networks, (ii) differentially expressed genes (DEGs) in APs, BPs and TTS and (iii) GO terms enriched within DEGs of electroporated cell scRNA-seq data. The analysis of changes in the TF network activity in response to DOT1L inhibition, in a cell-type resolved manner, was done using the SCENIC package (Aibar *et al*, 2017) that revealed a set of key transcriptional regulators with treatment and cell-type-specific activity changes (Figs 6A and EV5A). *Atf4*, *Cepbg*, *Ets1*, *2*, *Ezh2*, *JunB*, *Pou3f1*, *Pou32f2*, *Rad21*, *Sox2*, *4*, *9*, *11*, *21*, *Tcf7l1* and *Tcf4*, which were present in both treatment conditions, changed activity upon DOT1L inhibition in APs, BPs or TTS. Intriguingly, analysis of GO terms that were enriched in APs and BPs revealed that the DEGs upon DOT1L inhibition included metabolism and oxidative phosphorylation (OxPhos), a hallmark of neuronal differentiation, suggesting thus a potential alternative mechanism compared to spindle orientation (Fig EV3D and E). The DEGs in the TTS also enriched for GO terms, pointing not only towards metabolic changes but also towards a more differentiative state upon DOT1L inhibition compared to control (Fig EV3F, Appendix Fig S6).

We next correlated TF with altered activity and their respective targets with altered expression levels upon DOT1L inhibition in our data set. We used four filtering steps that we applied to the SCENIC output: (i) identification of TF with opposite activities in APs compared to TTS, (ii) selection of predicted targets with a high motif conformation, (iii) intersection of putative targets from both control and EPZ condition that passed the first two filtering steps and (iv) intersection of the TF targets with DEGs upon DOT1L inhibition in APs and TTS. This analysis retrieved 17 potential target genes, among which we found increased expression of three metabolic enzymes that are involved in producing intermediates that fuel, directly or indirectly, the TCA cycle, that is, *Asns*, *Gapdh* and *Hk2* (Fig 6B).

In this set of target genes, the increased expression of *Asns* was our top candidate as misexpression of *Asns* is not only involved in leukaemia (Lomelino *et al*, 2017) (for which deregulated functions of DOT1L have been described (Okada *et al*, 2005)) but its mutation also causes microcephaly (Ruzzo *et al*, 2013), and it is expressed

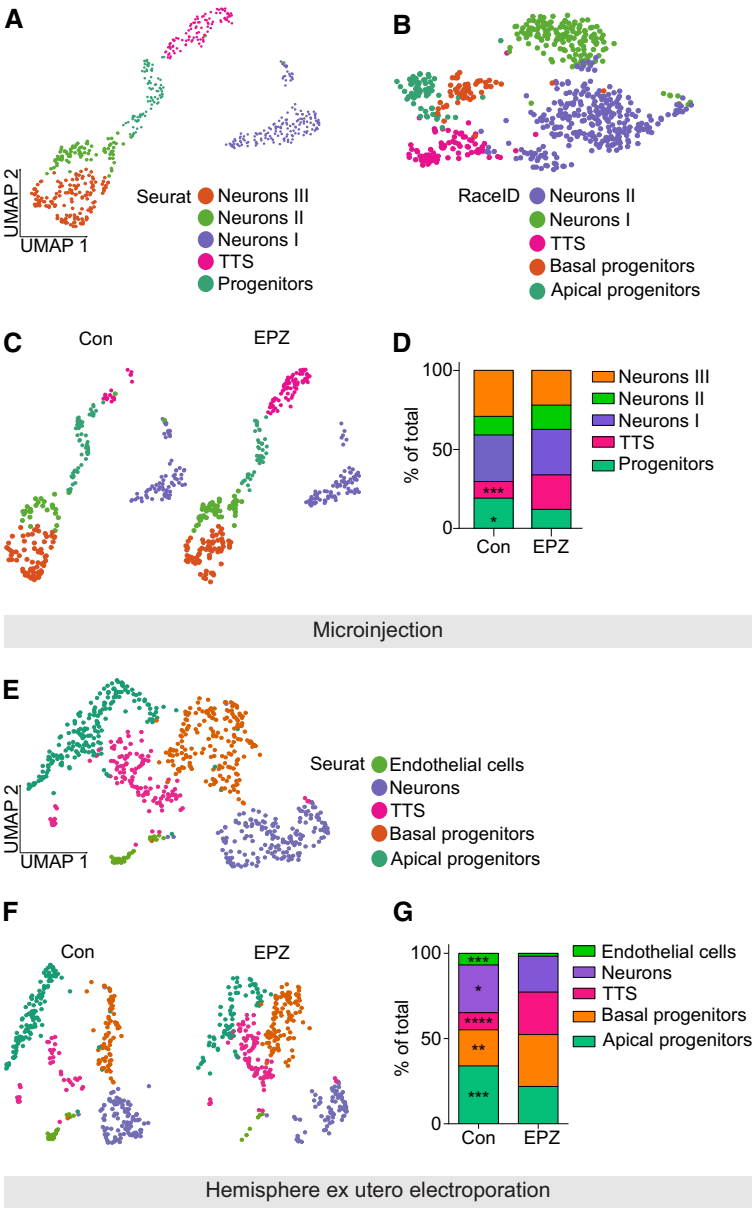

Figure 5. Single-cell transcriptome 24 h after AP labelling via microinjection or *ex utero* electroporation reveals a differentiative cell fate upon DOT1L inhibition.

A Two-dimensional representation (UMAP embedding) of clusters arising from Seurat analysis of scRNA-seq data from cells labelled via microinjection. A total of 589 cells were retrieved.

B Clusters retrieved via RaceID analysis of scRNA-seq data from a total of 639 cells labelled via microinjection represented in low dimension (t-SNE). Cells from both Con and EPZ conditions were combined for clustering analysis. Each dot represents a cell, and cells marked by a colour represent a specific cell state/type. Annotated cells (RaceID): APs (Con: 34 cells, EPZ: 33 cells), cells in TTS (Con: 26 cells, EPZ: 57 cells), BPs (Con: 29 cells, EPZ: 24 cells), neurons I (Con: 58 cells, EPZ: 92 cells) and neurons II (Con: 117 cells, EPZ: 169 cells).

C scRNA-seq clusters from microinjected cells split by condition (Con: 248 cells, EPZ: 341 cells). Annotated cells from microinjection data (Seurat v3): APs/BPs (Con: 48 cells, EPZ: 42 cells), cells in transient transcriptional state (TTS) (Con: 26 cells, EPZ: 74 cells), neurons I (Con: 73 cells, EPZ: 98 cells), neurons II (Con: 29 cells, EPZ: 52 cells) and neurons III (Con: 72 cells, EPZ: 75 cells).

D Fraction of cell states in microinjected cells expressed as percentage of total cells per condition. Fisher's exact test was performed. *$P < 0.05$, ***$P <$ 00.1.

E Low-dimensional representation (UMAP embedding) of clusters arising from Seurat analysis of scRNA-seq data from cells labelled via electroporation. A total of 711 cells were retrieved.

F scRNA-seq clusters from electroporated cells split by condition (Con: 350 cells, EPZ: 361 cells). Annotated cells from electroporation data (Seurat v3): APs (Con: 119 cells, EPZ: 79 cells), cells in TTS (Con: 35 cells, EPZ: 90 cells), BPs (Con: 74 cells, EPZ: 110 cells), neurons (Con: 98 cells, EPZ: 76 cells) and endothelial cells (Con: 24 cells, EPZ: 6 cells).

G Fraction of cell states in electroporated cells expressed as percentage of total cells per condition. Fisher's exact test was performed. *$P < 0.05$, **$P < 0.01$, ***$P < 0.001$, ****$P < 0.0001$.

Source data are available online for this figure.

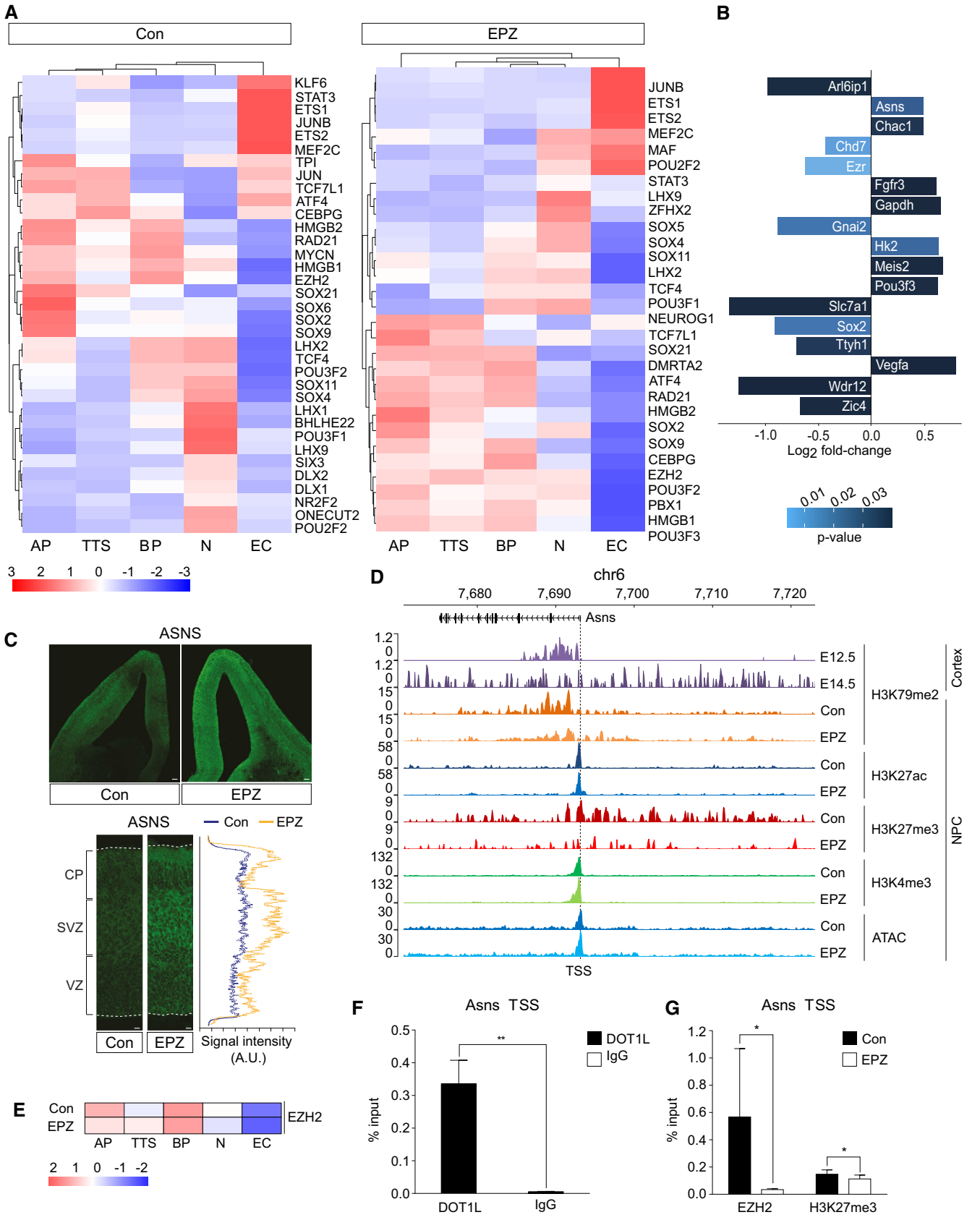

Figure 6.

Figure 6. DOT1L inhibition leads to PRC2 de-repression of *Asns* gene locus in neural progenitors.

A Heatmap of results from SCENIC analysis showing activities of regulons and transcription factors controlling them in control (left) and EPZ (right)-treated condition, resolved according to cell type/state. Scale represents enrichment scores for regulons expressed as area under recovery curve (AUC) of gene expression value-based rankings across all genes for each cell.

B DEGs upon DOT1L inhibition in APs and TTS directly targeted by transcription factors captured in the SCENIC analysis. Given is the $\log_2$FoldChange of the respective DEG and as shades of blue the *P*.adjust value.

C Immunostaining showing ASNS-positive cells in the VZ, SVZ and CP of control and EPZ-treated sections; and signal intensity for each condition. Scale bars: 50 μm. Dotted lines mark either ventricular or pial surface of the tissue.

D ChIP-seq and ATAC-seq tracks showing distribution of peaks for selected chromatin marks on the *Asns* locus for NPCs and cerebral cortex of E12.5 and E14.5 mice. Tracks for control and EPZ conditions are compared in NPCs. Indicated is the TSS of *Asns*.

E Comparison of the activity patterns of regulons controlled by EZH2 upon EPZ inhibition and in controls, resolved according to cell type/state. Scale as in A.

F ChIP–qPCR analysis for DOT1L and IgG ($n = 7$; biological replicates) at the TSS on *Asns* genomic locus in *in vitro*-derived NPCs. One-sided paired Wilcoxon statistical test was performed, error bars represent SEM. $^{**}P < 0.01$.

G ChIP–qPCR analyses for EZH2 ($n = 5$; biological replicates) and H3K27me3 ($n = 9$; biological replicates) at the TSS on *Asns* genomic locus in control and EPZ-treated condition of *in vitro*-derived NPCs. One-sided paired Wilcoxon statistical test was performed, error bars represent SEM. $^{*}P < 0.04$.

Source data are available online for this figure.

during cortical development (Fig EV5B and C). However, DOT1L is generally considered to favour transcription, thus increased expression of ASNS upon DOT1L inhibition, as confirmed on the protein level (Fig 6C), is seemingly counter-intuitive. To gain insight into the mechanism that increased expression levels of *Asns* upon DOT1L inhibition, we made use of an extensive quantitative epigenetic data set of mouse embryonic stem cells-derived NPCs (Ferrari *et al*, 2020). The ChIP-seq profiles from NPCs at the *Asns* gene locus revealed specifically decreased levels of H3K27me3 alongside decreased levels of H3K79me2 upon DOT1L inhibition (Fig 6D). This epigenetic profile suggested that PRC2 de-repression resulted in increased expression levels of *Asns* upon DOT1L inhibition in NPCs. In line with this hypothesis, the gene regulatory network with altered activity upon DOT1L inhibition, in our tissue paradigm, included EZH2 (Fig 6A and E). ChIP–qPCR using NPCs showed that DOT1L was present at the *Asns* promoter (Fig 6F) and that DOT1L inhibition reduced the presence of EZH2 and the level of H3K27me3 at the TSS of the *Asns* gene locus (Fig 6G). Taken together, these data suggest the presence of a local regulatory network in which a lower activity of DOT1L results in lower activity of EZH2 at the *Asns* gene locus that causes less H3K27me3 at the TSS of *Asns*, increasing its expression. Our data thus provide a mechanistic link between DOT1L inhibition and increased expression of target genes.

DOT1L affects lineage progression by regulating AP metabolism in an ASNS-dependent manner

To assess if *Asns* was functionally involved in the cellular phenotype we observed upon DOT1L inhibition, we examined if ASNS inhibition would rescue the EPZ-induced premature differentiation of APs. We labelled APs by *ex utero* electroporation of a mCherry reporter plasmid and incubated the hemispheres for 24 h with DMSO (control), or with EPZ, either with or without L-Albizziine (L-Alb), an inhibitor of ASNS (Fig 7A and B). We assessed the extent of neurogenesis and differentiation using co-immunostainings for TUBB3 (Fig 7A). In line with our previous data (Fig 3B and F), we observed an increase in TUBB3-expressing cells in the electroporated cells upon DOT1L inhibition (Fig 7B). The increased neuronal differentiation upon EPZ treatment was completely abolished by co-inhibition of the ASNS activity (Fig 7B). We next examined if the altered expression of *Asns* might be a key driver of AP's neuronal differentiation *per se*. We hence overexpressed ASNS together with a GFP reporter using *ex utero* electroporation and analysed the TUBB3 expression in the electroporated cells (Fig 7C). Upon overexpression of ASNS in APs, we observed twice as many TUBB3-positive cells compared to control (Fig 7D). Finally, we used *in utero* electroporation to overexpress ASNS in the developing cerebral cortex. This *in vivo* experimentation retrieved increased numbers of TBR1-positive neurons upon overexpression of ASNS, confirming that asparagine metabolism is a critical regulator of neuronal differentiation of APs (Fig 7E and F).

Thus, taken together, pharmacological and genetic perturbation data show that the differentiative role of DOT1L in APs is mediated by an ASNS-dependent metabolic regulation.

Discussion

In this study, we investigate the impact of DOT1L enzymatic activity in regulating neural progenitor behaviour during neurogenesis by combining pharmacological inhibition of DOT1L with single-cell tracing in tissue, high-resolution lineage reconstruction and transcriptomic profiling of lineage-related cells. Our data suggest that DOT1L inhibition changes the mode of division of APs, the founder progenitor population of the neocortex, resulting in an increase in neuronal differentiation. Highly resolved lineage tracing and analysis show that DOT1L inhibition seemingly favours symmetric consumptive division (APs giving rise to two neurons) over asymmetric self-renewing division (APs giving rise to one AP and one BP). To the best of our knowledge, this is the first transcriptional regulator described altering AP's division mode in this manner. Transcriptional profiling reveals that DOT1L influences fate transition by regulating crucial metabolic enzymes of the asparagine pathway in APs. Our findings thus correlate the epigenetic landscape of neural progenitors, their metabolic state and fine-cell biological processes leading to delamination and fate transition.

In our work, we make use of highly resolved cell biological analyses in tissue, and we focus our attention on the division mode, cellular output and delamination as they represent the different faces of a much broader repertoire of processes defining cell identity and driving fate transition. Extending on previous findings (Franz *et al*, 2019; Ferrari *et al*, 2020), our present data strongly suggest that

DOT1L activity preserves asymmetric self-renewing divisions of APs and in turn prevents delamination. Of note, also BPs upon DOT1L inhibition might enter the transient state that resolves towards neurons. How DOT1L affects the fate asymmetry of division and cell delamination remains an open question. One possibility might be that H3K79 methylation serves as epigenetic memory of an AP fate and that DOT1L activity is needed to keep the progenitor state (or the asymmetry of it after mitosis) similar to what has been shown using *in vitro* differentiation models of stem cells (Ferrari *et al*, 2020; preprint: Hergenreder *et al*, 2022). Given that H3K79 methylation is a relatively stable histone mark, erased rather through cell division than demethylation (Chory *et al*, 2019), a memory and barrier function for fate switching of H3K79 methylation would be an ideal feature.

In addition to H3K79me2, we here provide novel mechanistic insight into a local DOT1L/PRC2 crosstalk reminiscent of the local epigenetic signature associated with promoters of genes with increased expression upon DOT1L inhibition in NPCs *in vitro* (Ferrari *et al*, 2020). In NPCs, genes that transcriptionally increase upon DOT1L inhibition associate with bivalent or PRC2-repressed promoters. Of note, the use of EPZ uncouples DOT1L activity from its scaffolding functions and therefore allows us to link the

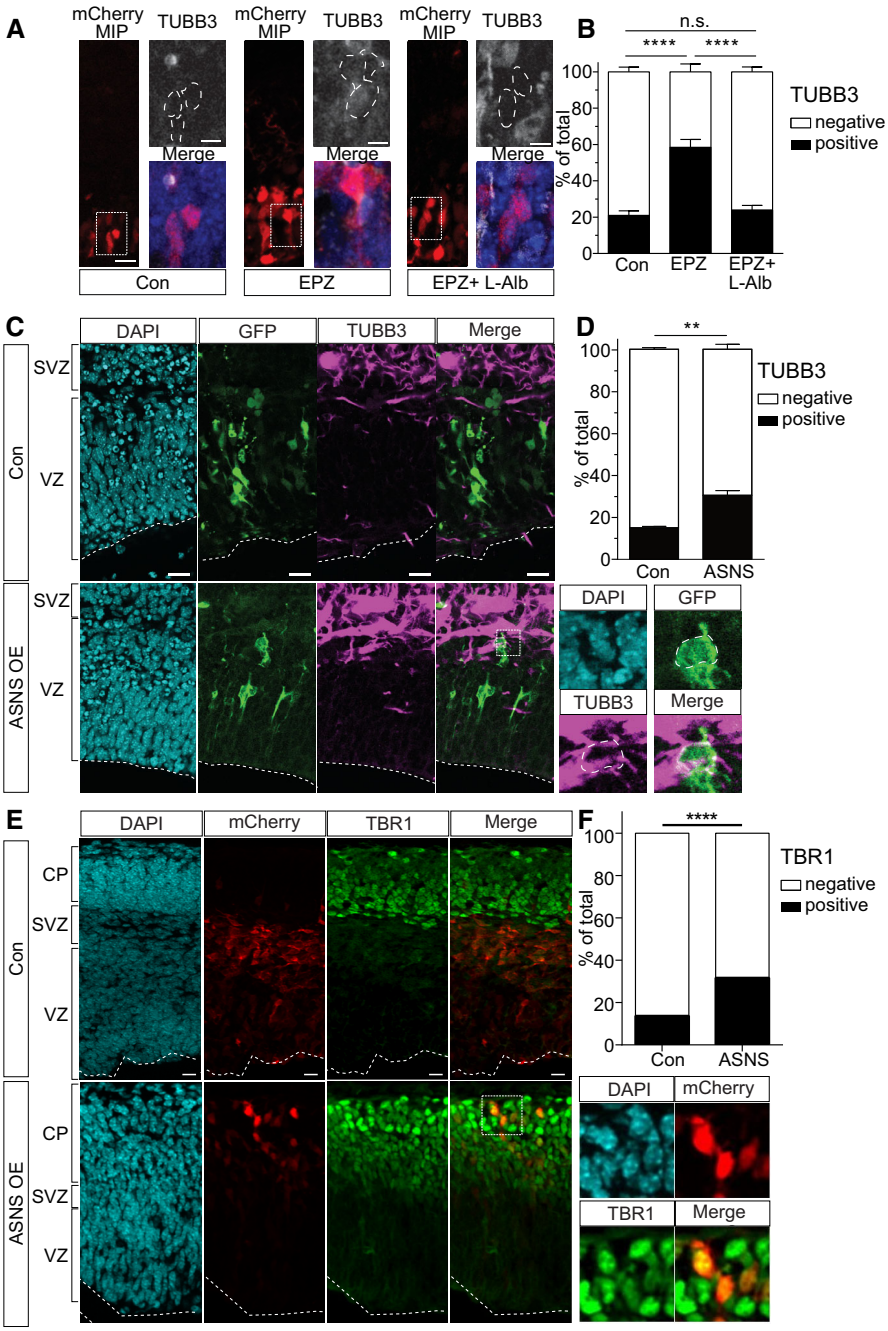

Figure 7.

Figure 7. Increased ASNS expression mediates differentiative effects in response to DOT1L inhibition.

A Overview of mCherry-positive cells in IF staining for TUBB3 in control (Con), EPZ and co-inhibition (EPZ + L-Albizziine (L-Alb)) conditions. Scale bars in main panels: 200 μm, in insets: 50 μm.

B Fraction of TUBB3-positive and -negative cells expressed as percentage of total cells per condition. Quantifications were made from independent experiments ($n = 3$), 183 cells in total (Con: 118 cells, EPZ: 182 cells, L-Alb/EPZ: 174 cells). Fisher's exact test, ****$P < 0.0001$, error bars represent SEM. MIP—maximum-intensity projections.

C *Ex utero* electroporated cells expressing GFP (green) or TUBB3 (magenta) in control (Con; pCMV-GFP) or in ASNS overexpression (ASNS OE; pCMV-ASNS-GFP) condition 24 h after slice culture. Scale bars: 20 μm. Dotted lines mark ventricular surface of the tissue. Magnifications on the right show exemplarily a GFP and TUBB3 double-positive cell upon ASNS overexpression. Dotted shapes indicate the border of cell soma based on GFP expression.

D Fraction of TUBB3-positive and -negative cells expressed as percentage of total cells in Con and upon ASNS OE. Quantifications were made from independent experiments ($n = 3$). Student's *t*-test, **$P < 0.01$, error bars represent SEM.

E Representative images of mCherry (red) or TBR1-expressing (green) cells in control (Con; pCAG-mCherry) or in ASNS overexpression (ASNS OE; pCAG-ASNS) condition 48 h after *in utero* electroporation. Scale bars: 20 μm. Dotted lines mark ventricular surface of the tissue. Magnifications on the right show exemplarily mCherry and TBR1 double- or single-positive cells upon ASNS overexpression.

F Fraction of TBR1-positive and -negative cells expressed as percentage of total cells in Con and upon ASNS OE. Quantifications were made from 1,141 cells in control group and 606 cells in ASNS OE group. Fisher's exact test, ****$P < 0.0001$.

Source data are available online for this figure.

molecular and cellular phenotype(s) specifically with the methyltransferase activity of DOT1L. We present here evidence that DOT1L enzymatic activity affects PRC2 activity in cortical tissue. DOT1L inhibition leads to reduced activity of the PRC2 member EZH2 in APs compared to control.

Our data thus suggest that, in control condition, higher EZH2/PRC2 activity in APs compared to neurons is associated with maintenance or re-establishment of progenitor identity; in turn, lower activity levels lead to neuronal differentiation. In line with this hypothesis, APs with *Eed* or *Ezh2* loss of function were found to have an accelerated and precocious cell cycle exit (Pereira *et al*, 2010; Telley *et al*, 2019).

Our data contribute to strengthening the concept that PRC2 activity is of major importance for preserving AP identity and self-renewal potential. And, regarding the crosstalk with PRC2, DOT1L inhibition in this context reduced binding of EZH2 and H3K27me3 levels in NPCs *in vitro*. Notably, the acute and strong reduction in EZH2 might not be directly followed by a comparable reduction in H3K27me3, as shown in Fig 6G. H3K27me3 can be erased either by cell division or by demethylases, which are two processes that might have slower kinetics than the recruitment of EZH2 at the respective genomic loci.

Interestingly, DOT1L/PRC2 crosstalk takes place in other cell types, in which transcripts increase upon DOT1L inhibition (Aslam *et al*, 2021). In immune cells, the proposed underlying mechanism is transcriptional decrease in *Ezh2* upon DOT1L loss of function (Aslam *et al*, 2021). In our lineage-resolved scRNA-seq data, however, *Ezh2* transcription did not change upon DOT1L inhibition in APs, TTS or BPs (see Dataset EV1), but its activity was altered. DOT1L/PRC2 crosstalk might, therefore, have different facets depending on the cell type.

Interestingly, we here identified *Asns* as one DOT1L/PRC2 target and crucial partner in the regulative network affecting AP differentiation. By identifying *Asns*, we here describe a previously unknown link among metabolism, epigenetics and APs, and strengthen the concept that metabolism is a crucial regulator of stem and progenitor cells.

Asns encodes for asparagine synthetase, an enzyme that converts glutamine (Gln) and aspartate (Asp) to glutamate (Glu) and asparagine (Asn). Glu can be further metabolised to 2-oxo-glutarate, feeding the TCA cycle and fostering mitochondrial energy supply through OxPhos (Zheng *et al*, 2016; Shiratori *et al*, 2019). ASNS might be crucial to balance not only the abundance of important amino acids used for protein synthesis but might also feed into other metabolic processes including the TCA cycle. The importance of the TCA cycle and mitochondrial metabolism is highlighted by recent findings showing that ARHGAP11B, a human-specific gene involved in cortical expansion, mediates glutaminolysis and increases the Glu levels that feed the TCA cycle (Namba *et al*, 2020).

Intriguingly, ASNS dysfunction is linked to microcephaly (Ruzzo *et al*, 2013; Schleinitz *et al*, 2018). It should be noted that *Asns* loss of function (Ruzzo *et al*, 2013), as well as *Asns* overexpression (this study), seems to produce microcephalic features. *Asns* expression is lower in progenitors compared to neurons, both in humans (Johnson *et al*, 2016) and in mice (Ruzzo *et al*, 2013). Thus, loss of function might affect neurons much more than progenitors, while overexpression might affect primarily APs, where low levels of *Asns* might be necessary to maintain their self-renewing potential.

The precise mechanisms linking the DOT1L-mediated increased ASNS expression to the regulation of AP behaviour are not yet clear. Based on the current literature, several options can be envisaged. On one hand, DOT1L inhibition and increased ASNS expression might alter Glu and/or Asp levels. Both amino acids can be metabolised to intermediates of the TCA cycle (2-oxo-glutarate and oxaloacetate), the activation of which could result in mitochondrial energy supply (OxPhos). OxPhos is the main energy source of cancer cells (Shiratori *et al*, 2019) and also of neurons (Zheng *et al*, 2016). On the other hand, Glu was reported to regulate stem and progenitor cells when released in the extracellular space, where it depolarises stem and progenitor cells, inhibiting DNA synthesis and favouring neurogenesis (LoTurco *et al*, 1995). Furthermore, Asn could also have a more direct role, by activating the mTOR pathway and/or acting as a sensor of specific cellular states or cell growth as reported for cancer cells (Krall *et al*, 2016, 2021). As little is known about direct functions of ASNS in APs, much more research is needed to clarify its precise role in APs.

The highly resolved lineage tracing showing the premature switch to symmetric consumptive divisions upon DOT1L inhibition also provides a likely cell biological explanation for microcephalic phenotypes associated with *ASNS* (Ruzzo *et al*, 2013) or *DOT1L*

mutations. Placing our work in a broader frame, it is interesting to note that while primary microcephaly mutations in *ASPM* or *MCPH1* are associated with premature switch from symmetric proliferative to asymmetric self-renewing division (Fish *et al*, 2006; Gruber *et al*, 2011), DOT1L inhibition is the first one reported to be associated with the premature switch from asymmetric self-renewing to symmetric consumptive division. This premature switch is likely to decrease the number of BPs generated, further reducing the total neuronal output. These observations highlight the role of symmetry versus asymmetry of AP's fate choice in defining the window of cortical neurogenesis and in affecting cortical development in physiology and pathology.

Materials and Methods

Reagents and Tools table

Reagent or resource	Source	Identifier
Primary antibodies		
Mouse monoclonal anti-dextran antibody, clone DX1 (dil 1:1000)	STEMCELL technologies	Cat# 60026
Rabbit anti-GFP (dil 1:500)	Abcam	Cat# ab6556
Goat anti-TUBB3 (dil 1:1000)	Everest biotech	Cat# EB11685
Rabbit anti-Tbr2 (dil 1:500)	Abcam	Cat# ab183991
Mouse anti-g-Tubulin (dil 1:500)	Sigma-Aldrich	Cat# T6557
Mouse anti-TuJ1 (1:1,000)	Covance Research Products	Cat# MMS-435P
Mouse anti-TuJ1 (dil 1:500)	Bio Legend	Cat# 801209
Rabbit anti-ARL13B	Proteintech Group	Cat# 17711-1-AP
Rabbit anti-H3K27me3	Active Motif	Cat# 39155
Rabbit anti-EZH2	Active Motif	Cat# 39901
Rabbit anti-DOT1L	Cell Signaling	Cat #77087
Rabbit anti-DOT1L	Atlas Antibodies	Cat # HPA074977
Normal rabbit IgG	Santa Cruz	Cat #sc2027
Rat anti-CTIP2 (dil 1:200)	Abcam	Cat# ab18465
Rabbit anti-H3K79me2 (dil 1:500)	Abcam	Cat# ab3594
Rabbit anti-ASNS (dil 1:500)	Sigma-Aldrich	Cat# HPA026109
Rat anti-PH3 (dil 1:500)	Abcam	Cat# ab10543
Goat anti-SOX2 (dil 1:200)	R & D Systems	Cat# AF2018
Secondary antibodies		
Donkey Anti-Rabbit IgG (H + L) Highly Cross-Adsorbed Secondary Antibody, Alexa Fluor 488	Thermo Fisher Scientific	Cat# A-21206
Donkey Anti-Rabbit IgG (H + L) Highly Cross-Adsorbed Secondary Antibody, Alexa Fluor 555	Thermo Fisher Scientific	Cat# A-31572
Donkey Anti-Mouse IgG (H + L) Highly Cross-Adsorbed Secondary Antibody, Alexa Fluor 488	Thermo Fisher Scientific	Cat# A-21202
Donkey Anti-Mouse IgG (H + L) Highly Cross-Adsorbed Secondary Antibody, Alexa Fluor 647	Thermo Fisher Scientific Thermo	Cat# A-31571

Reagents and Tools table (continued)

Reagent or resource	Source	Identifier
Donkey Anti-Goat IgG (H + L) Cross-Adsorbed Secondary Antibody, Alexa Fluor 647	Thermo Fisher Scientific	Cat# A-21447
Tissue culture supplies		
Rat serum	Charles River Lab., Japan	Cat# S-919-S
DMEM-F12, modified low glucose	Sigma	Cat# D2902
Dextran-Alexafluor 488 (10,000 MW anionic, fixable)	Invitrogen	Cat# D22913
Agarose, low melting point	Roth	Cat# 6351.2
B-27 supplement	Invitrogen	Cat# 17504-044
Cell matrix type 1-A	Kyowa chemical products	Cat# 631-00651
L-Glutamine (200 mM)	Thermo fisher scientific	Cat# 25030024
HEPES-NaOH (pH 7.2 1M)	Sigma-Aldrich	Cat# H3537
Slice/hemisphere culture incubation box	MPI-CBG workshop	N/A
Chemicals, peptides		
EPZ5676	Selleckchem	Cat# S7062
DMSO	Thermo Fisher Scientific	Cat# TS-20688
L-Albizziine	Gold Biotechnology	Cat# A-230-250
Phalloidin-Alexa 555	Molecular Probes	Cat# A34055
EdU (5-ethynyl-2′-deoxyuridine)	Thermo Fisher Scientific	Cat# A10044
Commercial assays		
Neural Tissue Dissociation Kit (P)	Miltenyi Biotec	Cat# 130-092-628
Click-it EdU Detection Kit	Molecular Probes	Cat# C10340
Deposited data		
Single-cell RNA-sequencing (scRNA-seq) data	This paper	GEO: GSE176323
Experimental models: Organisms/strains		
Wild-type mouse: C57BL/6JRj	Janvier Labs	N/A
Transgenic mouse: Tis21^{+}/tm2(Gfp)Wbh	Haubensak *et al* (2004)	N/A
Plasmids and Oligonucleotides		
pCAGGS-mCherry	Genscript	N/A
pCMV-ASNS-GFP	Origene	MG208883
pCMV-GFP	Origene	PS100010
PLKO.1 shDOT1L CCTCGGTTTACACAGCTTCAActcgagTTGAAGCTGTGTAAACCGAGG	Genscript	N/A
192 polyT primers with unique molecular index and cell barcode	Integrated DNA technologies	Sagar *et al* (2018)
DOT1L fw: CGAGCCCGCCGTCTAC	Sigma	N/A
DOT1L rv: GTCTCAATAATCTCATGAGCAGC	Sigma	N/A
ASNS_TSS_fw: TCCCGCTTACCTGAGCACTA	Sigma	N/A
ASNS_TSS_rv: CAGCCACATGATGAAACTTCC	Sigma	N/A
randomhexRT primer, GCCTTGGCACCCGAGAATTCCANNNNNN	Integrated DNA technologies	Sagar *et al* (2018)
RNA PCR Primers, sequences available from Illumina (RP1, RPI1-RPI12, TruSeq)	Integrated DNA technologies	Sagar *et al* (2018)
Tissue and hemisphere culture supplies		
40% O_2, 55% N_2 and 5% CO_2	Airliquide	N/A

Reagents and Tools table (continued)

Reagent or resource	Source	Identifier
Sodium hydroxide pellets	Merck	Cat# 106482
Tyrode's salt	Sigma-Aldrich	Cat# T2145-10x1L
Sodium bicarbonate	Merck	Cat# 106323
Penicillin–Streptomycin	Gentaur	Cat# PAA P11-010
Lipofectamine™ LTX	Invitrogen	Cat #15338100
Optimem	Gibco	Cat # 31985-062
RevertAid Reverse Transcriptase	Thermo Fisher Scientific	Cat # EP0441
Software and algorithms		
RaceID3	v0.1.6	https://github.com/dgrun/RaceID3_StemID2_package
RStudio	v.3.6.1	https://www.rstudio.com/
R	v1.2.5042	https://www.r-project.org/
Seurat	v.3.1.2	https://satijalab.org/seurat/
Scran	v3.12	https://bioconductor.org/packages/release/bioc/html/scran.html
SingleCellExperiment	v1.8.0	https://www.bioconductor.org/packages/release/bioc/html/SingleCellExperiment.html
SCENIC	v1.1.2	https://github.com/aertslab/SCENIC
GENIE3	v1.12.0	https://github.com/aertslab/GENIE3
RcisTarget	v1.10.0	https://www.bioconductor.org/packages/release/bioc/html/RcisTarget.html
AUCell	v1.12.0	https://bioconductor.org/packages/release/bioc/html/AUCell.html
Bioconductor	v3.12	https://www.bioconductor.org/
clusterProfiler	v3.14.0	https://bioconductor.org/packages/release/bioc/html/clusterProfiler.html
Prism	v.8.0.	https://www.graphpad.com/scientific-software/prism/
Single-cell RNA-sequencing reagents and supplies		
RNaseOUT	Invitrogen	Cat# 10777-019
Superscript II	Invitrogen	Cat# 18064-014
Second Strand Buffer	Invitrogen	Cat# 10812-014
E. coli DNA ligase	Invitrogen	Cat# 18052-019
E. coli RNaseH	Invitrogen	Cat# 18021-071
E. coli DNA polymerase	Invitrogen	Cat# 18010-025
AMPure XP beads	Beckman Coulter	Cat# A63880
RNAClean XP beads	Beckman Coulter	Cat# A63987
MEGAscript T7 Transcription Kit	Invitrogen	Cat# AM1334
Phusion High-Fidelity PCR Master Mix with HF Buffer	NEB	Cat# M0531
ExoSAP-IT For PCR Product Clean-Up	Affymetrix	Cat# 78200
NEBNext Magnesium RNA Fragmentation Module	NEB	Cat# E6150S
randomhexRT primer, GCCTTGGCACCCGAGAATTCCANNNNNN	Integrated DNA technologies	Sagar *et al* (2018)
RNA PCR Primers, sequences available from Illumina (RP1, RPI1-RPI12 and TruSeq)	Integrated DNA technologies	Sagar *et al* (2018)
192 polyT primers with unique molecular index and cell barcode	Integrated DNA technologies	Sagar *et al* (2018)
Other		
scRNA-seq data analyses workflows	This paper	https://github.com/Vogel-lab/DOT1L_activity_neocortex-paper

Methods and Protocols

Mice

All animal studies were conducted in accordance with German animal welfare legislation, and the necessary licences were obtained from the regional Ethical Commission for Animal Experimentation of Dresden, Germany (Tierversuchskommission, Landesdirektion Dresden) or the Regierungspräsidium Freiburg (X-17/03S). Wild-type mice (C57BL/6J) were harvested at E14.5. Where specified, microinjection experiments were performed with *Tis21-Gfp* knock-in E14.5 mouse embryos. To obtain *Tis21-Gfp* knock-in mice, homozygous *Tis21-Gfp* knock-in male mice, Tis21^{+}/tm2(Gfp)Wbh (Haubensak *et al*, 2004), were mated with C57BL/6J females.

A schematic representation of all procedures and protocols involving the use of mice is shown in Appendix Fig S1.

Dissection and organotypic slice preparation

Mice pregnant with E14.5 embryos were sacrificed via cervical dislocation for litter harvesting. Embryos were transferred into ice-cold phosphate-buffered saline (PBS), decapitated and heads collected in ice-cold PBS for *ex utero* electroporation. For microinjection, heads of embryos were dissected in pre-warmed Tyrode's solution (37°C) for organotypic slice preparation as previously described (Taverna *et al*, 2012; Wong *et al*, 2014). Two-hundred-fifty micrometre vibratome sections were prepared and transferred into pre-warmed slice culture medium (SCM) (Taverna *et al*, 2012). The composition of the SCM is as follows: Neurobasal medium (Thermo Fisher Scientific, Germany), 10% rat serum (Charles River, Japan), 2 mM L-glutamine (Thermo Fisher Scientific), Penstrep (Thermo Fisher Scientific), N2 supplement (Thermo Fisher Scientific), B27 supplement (Thermo Fisher Scientific) and 10 mM Hepes-NaOH pH 7.3. Before the start of microinjection, brain slices were transferred to 3.5 cm dishes containing 37°C warm CO_2-independent microinjection medium (CIMM: DMEM-F12 (Sigma, Germany, D2906), 2 mM L-glutamine, Penstrep, N2 and B27 supplements, 25 mM final concentration and Hepes-NaOH pH 7.3).

Microinjection and slice culture

Microinjection into single APs in tissue was performed on organotypic slices from E14.5-developing mouse telencephalon. Depending on the purpose of the experiment, we used either manual or automated microinjection. Manual microinjection into single APs in tissue was used for lineage tracing experiments, following previously described protocols (Taverna *et al*, 2012; Wong *et al*, 2014). Automated microinjection into single APs in tissue was used for scRNA-seq experiments, where a higher throughput was needed (note that for the slices we planned to treat with EPZ, we selected slices that contained on average a higher number of microinjected cells). Automated microinjection was performed using Autoinjector 1.0, a recently developed high-throughput robotic platform (Shull *et al*, 2019, 2021). For all experiments, microinjection was performed in pre-warmed CO_2-independent microinjection medium (CIMM) (Taverna *et al*, 2012). Briefly, 1.5 µl of injection solution (5 µg/µl Dextran-Alexa488 or Dextran-Alexa555) was loaded into a microcapillary needle for microinjection. The microinjection needle was mounted on the capillary holder, and microinjection was performed either manually or with Autoinjector 1.0. by approaching the ventricular (apical) surface of organotypic tissue slices. Microinjected slices were embedded in a collagen matrix that was allowed to solidify at 37°C for 5 min. After this time, each dish received 2 ml of either SCM-containing 0.09% dimethyl sulfoxide (DMSO, Control, Con) or 9 nM DOT1L inhibitor Pinometostat (EPZ5676, EPZ) (Selleckchem, USA), and slices were transferred and kept in culture at 37°C in a humidified atmosphere of 40% O_2 / 5% CO_2 / 55% N_2. Unless stated otherwise, organotypic slices were kept in culture for 24 h, a time window corresponding to one complete cell cycle of APs at mid-neurogenesis (Arai *et al*, 2011).

Ex utero electroporation and hemisphere rotation culture

Ex utero electroporation of E14.5 mouse embryos was performed in sterile PBS. An intraventricular injection of a solution containing 1–1.5 µg/µl pCAG-GFP, pCAG-mCherry, pCMV-GFP (PS100010, Origene, USA) or pCMV-ASNS-GFP (MG208883, Origene) mixed with 0.1% Fast Green in sterile PBS was performed. It was immediately followed by 5–6 pulses of 28–30 V, 50 ms each at 1 s intervals delivered through platinum tweezer electrodes (3 mm diameter) using a BTX ECM830 electroporator, similar to what previously described (Calegari *et al*, 2002). Subsequently, electroporated hemispheres were dissected and placed in flasks containing 2 ml of SCM, where indicated with either EPZ or DMSO, for 24 h at 37°C and gentle rotation in a humidified atmosphere of 40% O_2 / 5% CO_2 / 55% N_2. For EdU pulse labelling, 1 µg/ml EdU was added to the SCM 1 h before the end of a 24 h slice culture. At the end of the culture, hemispheres were washed in 1× sterile PBS to remove media and processed for immunohistochemistry, or dissociated and processed by FACS followed by scRNA-seq. For ASNS/DOT1L co-inhibition experiments, electroporation of pCAG-mCherry was performed as described above using a NEPA21 super electroporator (Nepagene, Japan). Electroporated hemispheres were dissected and placed in glass culture dishes containing 2 ml of SCM with three conditions: EPZ only, EPZ in combination with 4 mM L-Albizziine (GoldBio, USA) or DMSO only. At the end of the culture, hemispheres were washed in 1× sterile PBS, fixed and processed for immunofluorescence analysis.

In utero electroporation

Briefly, embryonic day E13.5 pregnant C57BL/6 mice were anaesthetised with isoflurane, and the uterine horns were exposed. For the ASNS OE experiments, E13.5 embryos were injected intraventricularly with a solution containing Fast Green (Sigma) in sterile PBS and either 1.5 µg/µl pCAG-mCherry or a mixture of pCAG-mCherry (0.5 µg/µl) and pCAG-ASNS (1.5 µg/µl) into the lateral ventricle. For the DOT1L KD experiments, E13.5 embryos were injected intraventricularly with a solution containing: Fast Green (Sigma) in sterile PBS and 2.5 mg/ml of total DNA: 0.7 mg/ml of pCAGGS-GFP and 1.8 mg/ml of plasmid (sh-Dot1l or sh-control). For electroporation, five pulses of 40 V for a pulse length of 50 ms at 950 ms intervals were applied (electrodes CUY650P1 (Sonidel Ltd.) connected to an electroporator (Nepagene, Japan)). The uterine horns were returned to the abdominal cavity, and the embryos were allowed to develop for 48 h. Mice for ASNS OE or DOT1L KD were sacrificed by cervical dislocation and embryos were harvested 48 h post-electroporation (E15.5). Subsequently, embryonic brains were dissected and fixed

in 4% paraformaldehyde (PFA) overnight at 4°C, incubated in a 15% and 30% sucrose solution for cryoprotection and embedded for cryosectioning.

Tissue dissociation and FACS sorting

Following hemisphere rotation culture, the cortices were dissected. The electroporated area was identified and isolated using an epifluorescence microscope and dissociated into single-cell suspensions using a Neural Tissue Dissociation kit (P) (Miltenyi Biotec, Germany) following the manufacturer's instructions. Microinjected slices were dissected, and the microinjected area was identified and isolated using an epifluorescence microscope, then dissociated for sorting with the same dissociation kit as described above. Enrichment of labelled cells was performed via FACS on a BD FACS Diva 8.0.2 (Appendix Fig S5A). Cells were sorted into 384-well plates containing 240 nl lysis buffer (Herman *et al*, 2018). Sorted plates were centrifuged at 2,000 *g* for 1 min at 4°C and immediately transferred into a −80°C freezer until processing for scRNA-seq.

Library preparation, single-cell RNA sequencing and data accessibility

Processing of sorted cells for scRNA-seq was performed as described (Hashimshony *et al*, 2016) with modifications based on the mCEL-Seq2 protocol (Herman *et al*, 2018). Briefly, 384-well plates containing sorted cells in lysis buffer were incubated for 3 min at 90°C and quickly cooled down to 4°C. cDNA was synthesised from RNA in each well by adding 160 nl of reverse transcription mix (Herman *et al*, 2018), followed by incubation for 1 h at 42°C. Heat inactivation of the reaction mix was performed for 10 min at 70°C. Synthesis of cDNA second strand was performed at 16°C for 2 h. cDNA from 96 wells was pooled for sample clean-up and *in vitro* transcription. This resulted in four sequencing libraries from a single 384-well plate. Libraries were sequenced (paired-end) on Illumina Hi-seq 2500 at a depth of ~150,000 reads per cell. Raw scRNA-seq data along with expression matrices have been submitted to the online repository Gene Expression Omnibus (GEO), accessible via GSE176323.

For scRNA-seq of microinjected cells, we pooled FACS-isolated cells from three different microinjection experiments, which were performed on three different days. ScRNA-seq of electroporated cells was done once using cells pooled from two to three different electroporation experiments, which were performed on three different days. For all scRNA-seq experiments, the statistical testing was performed using intra-sample comparisons, according to established bioinformatics pipelines (see below).

Fixation, embedding and sectioning

Fixation, embedding and sectioning were performed as described (Taverna *et al*, 2012; Gray de Cristoforis *et al*, 2020). Brain, hemispheres or slices were washed twice with PBS to remove culture media, followed by fixation with 4% paraformaldehyde in 120 mM sodium phosphate buffer pH 7.4 at room temperature for 30 min followed by 4°C overnight. When performing staining for H3K79me2 and ASNS, brains were fixed with 1% paraformaldehyde in 120 mM sodium phosphate buffer pH 7.4 at room temperature for 60 min to avoid over-fixation. Following fixation, brains, hemispheres and slices were washed thrice with 1× PBS.

Sectioning of microinjected slices (floating sections)

Coronal sections (50 μm) were prepared from microinjected slices on a vibratome (Leica VT1000S). All slices were collected in PBS and stored at 4°C for subsequent immunofluorescence staining.

Sectioning of electroporated brains and hemispheres (cryosections)

Electroporated brains and hemispheres were infiltrated with 30% sucrose at 4°C overnight prior to embedding in TissueTek tissue freezing medium (Leica Biosystems, Germany). 16 μm sections were cut using a cryostat (Leica Biosystems) and resulting sections were stored at −20°C for further processing.

Immunofluorescence staining

Floating sections were processed for immunofluorescence (IF) staining as previously described (Taverna *et al*, 2012). In brief, sections were permeabilised with 0.3% Triton-X100 (Carl Roth, Germany) in PBS for 30 min, followed by quenching in 0.2 M glycine buffer pH 7.4 for 30 min. The sections were washed three times with IF buffer, and incubated with primary antibodies diluted in IF buffer overnight at 4°C. Subsequently, sections were washed five times for 5 min each time with IF buffer. Secondary antibodies were diluted in IF buffer with DAPI (Carl Roth, Germany) as nuclear counterstain. Sections were incubated at room temperature for 1 h followed by washing (five times 5 min each) with IF buffer and then PBS. Stained sections were mounted in Mowiol (Sigma, Germany) and imaged. Cryosections were processed for IF staining as follows. Sections were dried for 5 min in a chemical hood, washed twice with 1× PBS, followed by permeabilisation with 0.3% Triton-X100 (Carl Roth, Germany) in PBS for 30 min. Subsequently, sections were incubated with a blocking solution (10% Normal Donkey Serum and in 0.3% TritonX-100/PBS) for 1 h at room temperature in a humidified chamber. Primary antibodies diluted in blocking solution were incubated with the sections overnight at 4°C, followed by washing five times for 5 min each time with 0.3% Triton-X100 in PBS. Sections were then incubated with secondary antibodies diluted in blocking solution with DAPI as nuclear counterstain for 1 h at room temperature followed by washing five times 5 min each time.

For the DOT1L staining, the following modifications to the above-described protocol were implemented: (i) cryosections were subjected to antigen retrieval at 80°C for 1 h, as described in Arai *et al* (2011), (ii) the immunofluorescence buffer contained 1% TritonX-100/PBS (instead of 0.3%) and (iii) the primary antibody against DOT1L (Atlas Laboratories) was diluted in blocking solution and incubated with the sections for 48 h at 4°C.

A complete list of all primary and secondary antibodies used together with corresponding concentrations are listed in Reagents and Tools table.

Single-molecule (sm)FISH

smFISH was done with RNA BaseScope (ACDbio, USA) following the manufacturer's protocol. 16 μm cryosections were incubated for 45 min at 40°C in a humidified incubation chamber—Hybez II oven (ACDbio, USA), subsequently washed 5 min in 1× PBS and treated with hydrogen peroxide for 10 min at room temperature. Target retrieval was performed in 1× target retrieval buffer. The section was further treated with RNA Scope protease III for 30 min at 40°C. Probes for *Ofd1* and *Nr2f1* (ACDbio, USA) were pre-warmed for

10 min at 40°C, and a dilution of 1:50 was applied to the slides, which were incubated for 2 h at 40°C in a humidified incubation chamber. Hybridisation was followed by three amplification steps with detection of fluorophore at 1:1,000 dilution.

N2A cell transfection with shDOT1L plasmid

N2A cells were plated at a density of 250,000 cells per well in six-well plates. Transfection was performed 24 h later using 2.5 μg of plasmid, 6.5 μl Lipofectamine LTX (Invitrogen) and 500 μl Optimem (Gibco) per well, added drop by drop. Twenty-four hours after transfection, GFP expression was confirmed and selection was started using 10 μg/ml Puromycin for 2 days. Afterwards, cells were washed in PBS, snap frozen in liquid nitrogen and kept at −80°C until reverse transcription was performed.

Reverse transcription and qRT–PCR

1 μg of total RNA was reverse transcribed using RevertAid MMuLV reverse transcriptase kit (Thermo Fisher Scientific). qRT–PCR analysis was performed on a CFX-Connect Real-Time PCR detection system (Bio-Rad) using GoTaq qPCR Master Mix (Promega). Primers used had an efficiency level of 111%. qRT–PCR results were analysed using the ΔΔCt method with GAPDH as internal standard.

Microscopy and figure preparation

Imaging was performed with confocal (Leica TCS SP8, Leica, Germany; Zeiss LSM 780 NLO; Zeiss, Germany) or wide-field fluorescence (Zeiss Axio Imager M2; Zeiss) microscopes. Images shown are 1 μm-thick single-optical sections unless stated otherwise. Confocal images were taken at either 63× or 40× magnifications. Immunofluorescence images of single-optical sections were quantified using Fiji (Schindelin *et al*, 2012). Final image panels were processed with Inkscape 1.0.2, Adobe Illustrator CS5.1 or Affinity Publisher 1.10.5.

Quantification procedure for labelled cells

Ex vivo *lineage tracing*

We used a combined panel of cell morphological parameters and marker expression to score labelled cells and progeny in tissue. Microinjected cells and their progeny were identified as cells positive for the microinjection dye upon inspection at the epifluorescence microscope. To assess cellular and morphological organisation and marker expression, all positive cells in an experiment were imaged at high resolution using confocal microscopy (see also above). Microinjected cells and their progeny were scored for the presence or absence of apical contact by matching the signal of injected cells and their morphology with the general tissue structure, revealed by DAPI staining (presence of contact: apical contact$^+$; absence of contact: apical contact$^-$). Symmetry (apical contact$^+$/apical contact$^+$; apical contact$^-$/apical contact$^-$) versus asymmetry (apical contact$^+$/apical contact-) of apical contact in daughter cell pairs was assessed. Numbers of cells with or without apical contact were calculated as a percentage of total microinjected cells scored.

Positive microinjected cells were scored for the immunoreactivity to the cytoskeletal protein tubulin beta 3 class III (TUBB3) and classified as negative (TUBB3-) or positive (TUBB3$^+$). Proportions of TUBB3$^+$ and TUBB3$^-$ were calculated as percentage of total microinjected (or electroporated for the electroporation experiments) cells per condition. The BP marker eomesodermin (EOMES) was used to score BP fractions arising after culture. Cells positive for EOMES were quantified as EOMES$^+$ and those negative for it were marked as EOMES$^-$. Proportions of EOMES$^+$ and EOMES$^-$ cells were calculated as for TUBB3, see above.

The cell's neurogenic potential was assessed by scoring cell's positivity to GFP in the *Tis21-Gfp* mouse neocortices (Haubensak *et al*, 2004; Wong *et al*, 2014). For the quantification of immunofluorescence intensity levels, the area of the nucleus of interphase cells was selected using the DAPI staining as a guide (Wong *et al*, 2014). Cells positive for GFP were marked as TIS21-GFP$^+$ and those negative for it were marked as TIS21-GFP$^-$. For the TIS21-GFP$^+$ cells, the GFP positivity was classified as faint if the intensity was in the lower 30% portion of the GFP positivity range. Proportions of TIS21-GFP$^+$ strong, TIS21-GFP$^+$ mild and TIS21-GFP$^-$ were calculated as percentage of total cells per condition. To assess symmetry versus asymmetry of cell lineages arising from APs, daughter cell pairs were assessed for expression of TUBB3 and EOMES as described above. Daughter cell pairs were scored as symmetric for TUBB3 expression, meaning both cells were positive for TUBB3 (TUBB3$^+$/TUBB3$^+$) or negative (TUBB3$^-$/TUBB3$^-$), or asymmetric for TUBB3 expression (TUBB3$^+$/TUBB3$^-$). Proportions of each scored group were calculated as a percentage of total daughter cell number. The same approach was used to score symmetric versus asymmetric inheritance of BP identity (symmetric: EOMES$^+$/EOMES$^+$ and EOMES$^-$/EOMES$^-$; asymmetric: EOMES$^+$/EOMES$^-$). All lineage tracing experiments were performed on a minimum of three biological replicates.

Immunostainings

Positive cells were scored for the immunoreactivities for EdU, SOX2, CTIP2, TUBB3 or TBR1 and either scored within and normalised to a 100 μm defined surface width of the cortex or expressed as % of total labelled or scored cells.

Profile plot

For the graphs shown in Figs 6C and EV1H, the ASNS or DOT1L/GFP (upon Con and EPZ conditions) stainings across the cortical wall were quantified using the profile plot tool of Fiji on a 100-μm-wide window. The window height was set to match the height of the cortical wall.

APs mitosis

The orientation of the cleavage plane in mitotic APs relative to the ventricular surface and the partitioning of the apical plasma membrane were determined in optical sections of mitotic APs cells stained for DNA and phalloidin (to visualise the membrane and cell's contour), following the protocol developed by Kosodo (Kosodo *et al*, 2004).

ChIP–qPCR

Neural progenitor cells (NPC)

ChIP–qPCR was performed from neural progenitor cells (NPCs) as previously described (Bovio *et al*, 2019; Ferrari *et al*, 2020), with minor changes in composition of buffers: Lysis buffer for EZH2 (10 mM EDTA; 50 mM TRIS–HCl pH 8; 0.2% sodium dodecyl sulphate (SDS) and 1× protease inhibitor), lysis buffer for H3K27me3 (10 mM EDTA; 50 mM TRIS–HCl pH 8; 1% SDS and 1× protease inhibitor), dilution buffer (20 mM TRIS–HCl; 2 mM EDTA;

150 mM NaCl and 1% Triton). All ChIP–qPCR experiments performed with NPCs were generated from V6.5 mESCs as described (Ferrari *et al*, 2020), cultured on 1 × 10 cm cell culture dishes and treated for 48 h with 10 μM EPZ or 0.1% DMSO as control. Approximately 6 million cells were used in each ChIP experiment. 3 μg of IgG (#2027, Santa Cruz), 5 μg of H3K27me3 (#39155, Active Motif, USA), 5 μg of EZH2 (#39901, Active Motif) or 3 μg of DOT1L (#77087, Cell Signaling) antibody was used. Significant differences in H3K27me3 and EZH2 binding to the selected locus were calculated between EPZ and control using a one-sided paired Wilcoxon statistical test. Results from NPC ChIP–qPCR experiments are from a minimum of five independent replicates. The following primers targeting the transcriptional start site (TSS) on *Asns* were used:

ASNS_TSS_fw: TCCCGCTTACCTGAGCACTA
ASNS_TSS_rv: CAGCCACATGATGAAACTTCC

Bioinformatics analysis

All bioinformatics analyses are reproducible and stored as R scripts and markdown files on the online repository Github, accessible via: https://github.com/Vogel-lab/DOT1L_activity_neocortex-paper.

Alignment, transcript quantification and single-cell gene expression matrix

Alignment of paired-end reads to the murine transcriptome (Encode VM9 release, downloaded from the UCSC genome browser) was done using bwa (v0.6.2-r126) as previously published (Li & Durbin, 2009) with default parameters. Different isoforms of the same gene were merged into one gene locus. Reads mapping to multiple loci were excluded. A total of 750 cells (Con: 371, EPZ: 379) were recovered from *ex utero* electroporation experiments for sequencing. Cells from two microinjection experiments were pooled. The first experiment recovered 213 (Con: 59, EPZ: 154) cells. More slices were injected for the second experiment, which increased the number to 533 recovered cells (Con: 248, EPZ: 285). Cells from both microinjection experiments were pooled. A total of 746 (Con: 307, EPZ: 439) cells were recovered from the two microinjection experiments combined. In both *ex utero* electroporation and microinjection experiments, 34,205 genes were retrieved with 7 and 18 cells not passing the sequencing, respectively, due to low read quality. Batch effects were negligible in the pooled cells from the microinjection experiments, as the cells from both experiments clustered together and were represented in all clusters. Transcripts were assigned to single cells using information from barcodes on the left read, with the first six bases representing UMI and the next six bases corresponding to cell-specific barcodes (Herman *et al*, 2018). Counts for each transcript per cell were obtained by aggregating the number of UMIs per transcript mapping to each gene locus, and based on binomial statistics, the number of observed UMIs was converted into transcript counts (Grün *et al*, 2014). Subsequently, a single-cell transcript count matrix was constructed with row and column names corresponding to genes and cells respectively.

scRNA-seq data analysis with Seurat v3.0

All analyses with Seurat v3.0 (Stuart *et al*, 2019) were done separately for microinjection and electroporation data sets in R (v3.6.1) and Rstudio (v1.2.5042). Count matrices for microinjection and electroporation data sets were loaded and converted into SingleCellExperiment objects. Additional Bioconductor packages were used in combination with Seurat. Data processing steps and parameters, unless stated otherwise, were kept the same for both data sets. All data pre-processing and clustering steps were performed on a combined matrix containing cells from both conditions (Con and EPZ). Cells from the different experimental techniques (electroporation/microinjection) were analysed separately but with Con and EPZ cells combined into one matrix. All genes with row sums greater than zero were kept as expressed genes. Subsequently, total counts and distribution of counts for cells in both control and EPZ conditions were calculated. Quality control was performed using Scater (McCarthy *et al*, 2017), resulting in 17,456 and 17,192 expressed genes for electroporation and microinjection data sets respectively. Cells were filtered by excluding all those with a library size below 2,500 total transcript counts. This excluded 15 cells (electroporation) and 89 cells (microinjection) from further analysis. The next filtering step excluded all cells with expressed features (genes) below 1,000 (i.e. 1 cell from electroporation and 29 cells from microinjection). Cells with outlier values for mitochondrial genes were identified based on the median absolute deviation from the median number of mitochondrial genes across all cells. This filtering step discarded 16 cells (electroporation) and 21 cells (microinjection), retrieving 711 (Con: 350, EPZ: 361) and 589 (Con: 248, EPZ: 341) high-quality cells for clustering analysis in electroporation and microinjection data sets respectively.

A total of 800 of the highly variable genes were selected for computing principal components. The top eight principal components (PC) were used for clustering cells from electroporation and microinjection data sets respectively. For the top eight PC, both data sets showed strong enrichment of low *P*-value features as suggested by a drop of the *P*-value from the JackStraw plot and the visible elbow in the Elbow plot (Appendix Fig S7A and B). Unbiased clusters were annotated to cell types using a combination of top-expressed features and published markers for cell types. In the microinjection data set, AP and BP clusters were not resolved as separate clusters using Seurat. Thus, the resolution parameter was varied between 0.4 and 1.2 in increments of 0.1 to achieve optimised clustering. The resulting clusters were compared to each other using the adjusted rand index (ARI). From the average silhouette and the ARI, a resolution of 0.4 seemed to be the most stable for both microinjection and electroporation data sets (Appendix Fig S7A and B). Increasing the number of PCs used for clustering to 10 in the microinjection data set did not resolve AP/BP clusters (Appendix Fig S7C). Increasing the resolution to 1.2 in the microinjection data set resulted in additional clusters created from the initial ones, but did not separate the AP/BP cluster (Appendix Fig S7D). Because of this limitation, microinjected scRNA-seq data were analysed with RaceID3 (see below). Differential expression analysis was done based on standard settings in Seurat. Fisher's exact test was computed on the contribution of treatment conditions to each cluster.

scRNA-seq data analysis with RaceID3

scRNA-seq data from the microinjection experiment (728 cells) were analysed also with RaceID3, with minor adaptations to the default parameters (Herman *et al*, 2018). Before the filtering step, low-quality cells as previously identified (Grün *et al*, 2016) were

discarded. Filtering was done with the following parameters: mintotal = 2,500, minexpr = 10, minnumber = 5 and ccor = 0.4. Subsequent steps in RaceID3 analysis were run with the following parameters: metric = spearman, cln = 5, sat = False and outlg = 10. Marker genes for each cluster, intra-cluster differentially expressed genes (EPZ vs. DMSO control), as well as global differentially expressed genes between EPZ versus DMSO control were extracted using default settings in RaceID3. Following quality control and filtering of scRNA-seq data from the microinjection experiment, 639 cells (DMSO: 264, EPZ: 375) passed the quality control and filtering step for clustering and further downstream analysis. Fisher's exact test was computed on the contribution of treatment conditions to each cluster.

Single-cell regulatory network inference and clustering (SCENIC) analysis

Gene regulatory network activity (GRN) in each cell was computed with SCENIC as previously described (Aibar *et al*, 2017). SCENIC works in three steps: (i) prediction of transcription factors (TFs) and their target genes based on their co-expression in scRNA-seq data, (ii) checking for direct binding motifs of the TFs in the target genes and performing motif enrichment analysis using RcisTarget, and (iii) activities of the resulting Gene Regulatory Networks (GRN) also called regulons are scored for each cell. This tool takes Seurat objects as input. Seurat objects were exported after clustering analysis of the electroporation data set and divided into separate objects for control and EPZ cells respectively. Default settings were used for building the co-expression network and creating regulons. The top 50% of regulons were used in the GRN activity scoring. Heatmaps of the GRN activities per cell were generated using pheatmap (v1.0.12). Since each GRN is controlled by one TF, GRN activity and TF activity are used interchangeably here.

Selection of target genes

SCENIC outputs were explored further to narrow down potential target genes of DOT1L activity in our data. The regulon analysis step outputs a table containing TFs, their target genes, predicted binding motifs, whether the TFs bind with high conformity and a calculated normalised enrichment score (NES). TFs with high conformity predicted binding motifs in their target genes were selected. Among the selected TFs, those showing changed patterns of activity upon DOT1L inhibition were extracted. The resulting list of genes were intersected with DEGs from each cluster and this list was kept as TF target genes with altered expression upon DOT1L inhibition.

Trajectory inference analysis with Slingshot, Monocle3, scVelo and FateID

To infer differentiation trajectories in control and EPZ-treated cells, two approaches were employed. Slingshot and Monocle3 (Street *et al*, 2018; Cao *et al*, 2019) consider only spliced counts when computing trajectories. On the other hand, RNA velocity using scVelo (La Manno *et al*, 2018; Bergen *et al*, 2020) is based on the proportion of spliced and unspliced reads. All pre-processing and clustering steps are the same as for the Seurat analysis already described above in this section. Prior to each analysis, the data were split into control and EPZ-treated cells, and the analysis was performed for each condition using the same parameters. Except for plotting parameters, default settings were used in both Slingshot and Monocle3 analyses. In addition, the AP cluster was selected as the starting point of the trajectory for the Monocle3 run.

Spliced counts were added to the final data exported for scVelo analysis. Filtering and normalisation were performed with default parameters with n_top_genes set to 5,000. Subsequently, the means and uncentred variances were computed for each cell across their nearest neighbours with n_neighbours set to 30 and n_pcs of 20. Finally, the dynamical mode was selected to run the velocity estimation.

FateID was used to infer cell lineage structure following RaceID3 analysis (Herman *et al*, 2018).

Gene ontology (GO) term analysis

Over-representation analysis was performed using the enrichGO function of ClusterProfiler (v4.2.2). The following parameters were used: OrgDB = org.Mm.eg.db, ont = CC (for cellular components) or BP (for biological process), pAdjustMethod = BH, pvalueCutoff = 0.05, qvalueCutoff = 0.05 and readable = TRUE. Subsequently, dot plots of the top GO terms were made ordering genes by gene ratio and adjusted *P*-values.

ChIP- and ATAC-seq analysis

ChIP- and ATAC-seq analysis was performed on previously published data, gene expression omnibus (GEO) series accession numbers GSE135318 for H3K79me2, H3K27me3 and H3K4me3, ATAC in NPCs (Ferrari *et al*, 2020), GSE95831 for H3K79me2 E12.5 cerebral cortex and PRJNA282071 for H3K79me2 E14.5 cerebral cortex (Franz *et al*, 2019). The mean of individual replicates was calculated with deepTools2 bigwigCompare with a bin size of 25 bp before subtracting the mean input signal from the corresponding mean ChIP signal. DeepTools2 pyGenomeTracks v3.5 was used to plot the reads over the displayed genomic regions (*Asns* chr6:7,670,648-7,751,776).

Data availability

The single-cell RNA-sequencing data from this publication have been deposited to the GEO database and assigned the identifier GSE176323 (https://www.ncbi.nlm.nih.gov/geo/query/acc.cgi?acc=GSE176323).

The Source Data images can be found at https://www.ebi.ac.uk/biostudies/bioimages/studies/S-BIAD646. The accession number is: S-BIAD646.

Expanded View for this article is available online.

Acknowledgements

The authors thank Francesco Ferrari for generating the used ChIP-seq data sets, and Annalisa Izzo for ChIP–qPCR expertise and shRNA Dot1l KD validation. We also thank the entire Vogel, Taverna and Kalebic labs for discussions and critical comments on the manuscript. We thank Sagar for help with sequencing. We thank Mareike Albert and Takashi Namba for the critical comments on the manuscript and fruitful discussion on the data. We are grateful to the Services and Facilities of the Max Planck Institute of Molecular Cell Biology and Genetics for the outstanding support provided, notably Jussi Helppi and his team at the Animal Facility, Jan Peychl and his team at the Light Microscopy Facility, and Julia Jarrels and Ina Nüsslein of the FACS facility. We are grateful to Nicola Maghelli and Francesca Casagrande of the Light

Imaging Facility of the Human Technopole for the outstanding support provided. Chiara Ossola and Martina Polenghi are Ph.D. students at the European School of Molecular Medicine (SEMM).

This study was supported by the German Research Foundation 322977937/GRK2344 (BA, CF, TV, DG, MT and HB) and SPP1937/GR4980/1 (DG and PZ). Open Access funding enabled and organized by Projekt DEAL.

Author contributions

Bismark Appiah: Conceptualization; data curation; formal analysis; validation; investigation; methodology. **Camila L Fullio:** Formal analysis; investigation; visualization; methodology. **Chiara Ossola:** Investigation; methodology. **Ilaria Bertani:** Investigation; methodology. **Elena Restelli:** Investigation; methodology. **Arquimedes Cheffer:** Investigation; methodology. **Martina Polenghi:** Methodology. **Christiane Haffner:** Investigation; methodology. **marta Garcia-Miralles:** Methodology. **Patrice Zeis:** Methodology. **Martin Treppner:** Methodology. **Patrick Bovio:** Methodology. **Laura Schlichtholz:** Methodology. **Aina Mas-Sanchez:** Methodology. **Lea Zografidou:** Methodology. **Jennifer Winter:** Methodology. **Harald Binder:** Methodology. **Dominic Grün:** Conceptualization; methodology. **Nereo Kalebic:** Supervision; investigation; methodology; writing – original draft; writing – review and editing. **Elena Taverna:** Conceptualization; supervision; investigation; visualization; methodology; writing – original draft; project administration; writing – review and editing. **Tanja Vogel:** Conceptualization; formal analysis; supervision; funding acquisition; writing – original draft; project administration; writing – review and editing.

Disclosure and competing interests statement

The authors declare that they have no conflict of interest.

References

Aibar S, González-Blas CB, Moerman T, Huynh-Thu VA, Imrichova H, Hulselmans G, Rambow F, Marine J-C, Geurts P, Aerts J *et al* (2017) SCENIC: single-cell regulatory network inference and clustering. *Nat Methods* 14: 1083 – 1086

Arai Y, Pulvers JN, Haffner C, Schilling B, Nüsslein I, Calegari F, Huttner WB (2011) Neural stem and progenitor cells shorten S-phase on commitment to neuron production. *Nat Commun* 2: 154

Arnold SJ, Huang GJ, Cheung AFP, Era T, Nishikawa SI, Bikoff EK, Molnar Z, Robertson EJ, Groszer M (2008) The T-box transcription factor Eomes/Tbr2 regulates neurogenesis in the cortical subventricular zone. *Genes Dev* 22: 2479 – 2484

Asami M, Pilz GA, Ninkovic J, Godinho L, Schroeder T, Huttner WB, Gotz M (2011) The role of Pax6 in regulating the orientation and mode of cell division of progenitors in the mouse cerebral cortex. *Development* 138: 5067 – 5078

Aslam MA, Alemdehy MF, Kwesi-Maliepaard EM, Muhaimin FI, Caganova M, Pardieck IN, van den Brand T, van Welsem T, de Rink I, Song JY *et al* (2021) Histone methyltransferase DOT1L controls state-specific identity during B cell differentiation. *EMBO Rep* 22: e51184

Bedogni F, Hodge RD, Elsen GE, Nelson BR, Daza RAM, Beyer RP, Bammler TK, Rubenstein JLR, Hevner RF (2010) Tbr1 regulates regional and laminar identity of postmitotic neurons in developing neocortex. *Proc Natl Acad Sci U S A* 107: 13129 – 13134

Bergen V, Lange M, Peidli S, Wolf FA, Theis FJ (2020) Generalizing RNA velocity to transient cell states through dynamical modeling. *Nat Biotechnol* 38: 1408 – 1414

Bjornsson HT (2015) The Mendelian disorders of the epigenetic machinery. *Genome Res* 25: 1473 – 1481

Bovio PP, Franz H, Heidrich S, Rauleac T, Kilpert F, Manke T, Vogel T (2019) Differential methylation of H3K79 reveals DOT1L target genes and function in the cerebellum In vivo. *Mol Neurobiol* 56: 4273 – 4287

Britanova O, de Juan RC, Cheung A, Kwan KY, Schwark M, Gyorgy A, Vogel T, Akopov S, Mitkovski M, Agoston D *et al* (2008) Satb2 is a Postmitotic determinant for upper-layer neuron specification in the neocortex. *Neuron* 57: 378 – 392

Calegari F, Haubensak W, Yang D, Huttner WB, Buchholz F (2002) Tissue-specific RNA interference in postimplantation mouse embryos with endoribonuclease-prepared short interfering RNA. *Proc Natl Acad Sci U S A* 99: 14236 – 14240

Cao S, Yu S, Li D, Ye J, Yang X, Li C, Wang X, Mai Y, Qin Y, Wu J *et al* (2018) Chromatin accessibility dynamics during chemical induction of pluripotency. *Cell Stem Cell* 22: 529 – 542

Cao J, Spielmann M, Qiu X, Huang X, Ibrahim DM, Hill AJ, Zhang F, Mundlos S, Christiansen L, Steemers FJ *et al* (2019) The single-cell transcriptional landscape of mammalian organogenesis. *Nature* 566: 496 – 502

Chory EJ, Calarco JP, Hathaway NA, Bell O, Neel DS, Crabtree GR (2019) Nucleosome turnover regulates histone methylation patterns over the genome. *Mol Cell* 73: 61 – 72

Clark EA, Rutlin M, Capano L, Aviles S, Saadon JR, Taneja P, Zhang Q, Bullis JB, Lauer T, Myers E *et al* (2020) Cortical RORβ is required for layer 4 transcriptional identity and barrel integrity. *Elife* 9: e52370

D'Angelo A, De Angelis A, Avallone B, Piscopo I, Tammaro R, Studer M, Franco B (2012) Ofd1 controls dorso-ventral patterning and axoneme elongation during embryonic brain development. *PLoS One* 7: e52937

Estivill-Torrus G, Pearson H, van Heyningen V, Price DJ, Rashbass P (2002) Pax6 is required to regulate the cell cycle and the rate of progression from symmetrical to asymmetrical division in mammalian cortical progenitors. *Development* 129: 455 – 466

Ferrari F, Arrigoni L, Franz H, Izzo A, Butenko L, Trompouki E, Vogel T, Manke T (2020) DOT1L-mediated murine neuronal differentiation associates with H3K79me2 accumulation and preserves SOX2-enhancer accessibility. *Nat Commun* 11: 1 – 13

Fish JL, Kosodo Y, Enard W, Paabo S, Huttner WB (2006) Aspm specifically maintains symmetric proliferative divisions of neuroepithelial cells. *Proc Natl Acad Sci U S A* 103: 10438 – 10443

Franz H, Villarreal A, Heidrich S, Videm P, Kilpert F, Mestres I, Calegari F, Backofen R, Manke T, Vogel T (2019) DOT1L promotes progenitor proliferation and primes neuronal layer identity in the developing cerebral cortex. *Nucleic Acids Res* 47: 168 – 183

Gabriel E, Wason A, Ramani A, Gooi LM, Keller P, Pozniakovsky A, Poser I, Noack F, Telugu NS, Calegari F *et al* (2016) CPAP promotes timely cilium disassembly to maintain neural progenitor pool. *EMBO J* 35: 803 – 819

Gray de Cristoforis A, Ferrari F, Clotman F, Vogel T (2020) Differentiation and localization of interneurons in the developing spinal cord depends on DOT1L expression. *Mol Brain* 13: 85 – 20

Gruber R, Zhou Z, Sukchev M, Joerss T, Frappart PO, Wang ZQ (2011) MCPH1 regulates the neuroprogenitor division mode by coupling the centrosomal cycle with mitotic entry through the Chk1-Cdc25 pathway. *Nat Cell Biol* 13: 1325 – 1334

Grün D, Kester L, van Oudenaarden A (2014) Validation of noise models for single-cell transcriptomics. *Nat Methods* 11: 637 – 640

Grun D, Lyubimova A, Kester L, Wiebrands K, Basak O, Sasaki N, Clevers H, van Oudenaarden A (2015) Single-cell messenger RNA sequencing reveals rare intestinal cell types. *Nature* 525: 251

Grün D, Muraro MJ, Boisset J-C, Wiebrands K, Lyubimova A, Dharmadhikari G, van den Born M, van Es J, Jansen E, Clevers H *et al* (2016) De novo prediction of stem cell identity using single-cell transcriptome data. *Cell Stem Cell* 19: 266 – 277

Hagey DW, Muhr J (2014) Sox2 acts in a dose-dependent fashion to regulate proliferation of cortical progenitors. *Cell Rep* 9: 1908 – 1920

Hashimshony T, Senderovich N, Avital G, Klochendler A, de Leeuw Y, Anavy L, Gennert D, Li S, Livak KJ, Rozenblatt-Rosen O *et al* (2016) CEL-Seq2: sensitive highly-multiplexed single-cell RNA-Seq. *Genome Biol* 17: 1 – 7

Haubensak W, Attardo A, Denk W, Huttner WB (2004) Neurons arise in the basal neuroepithelium of the early mammalian telencephalon: a major site of neurogenesis. *Proc Natl Acad Sci U S A* 101: 3196 – 3201

Haydar TF, Ang E, Rakic P (2003) Mitotic spindle rotation and mode of cell division in the developing telencephalon. *Proc Natl Acad Sci U S A* 100: 2890 – 2895

Heins N, Cremisi F, Malatesta P, Gangemi RMR, Corte G, Price J, Goudreau G, Gruss P, Gotz M (2001) Emx2 promotes symmetric cell divisions and a multipotential fate in precursors from the cerebral cortex. *Mol Cell Neurosci* 18: 485 – 502

Hergenreder E, Zorina Y, Zhao Z, Munguba H, Calder EL, Baggiolini A, Minotti AP, Walsh RM, Liston C, Levitz J *et al* (2022) Combined small molecule treatment accelerates timing of maturation in human pluripotent stem cell-derived neurons. *bioRxiv* https://doi.org/10.1101/2022.06.02.494616 [PREPRINT]

Herman JS, Sagar, Grün D (2018) FateID infers cell fate bias in multipotent progenitors from single-cell RNA-seq data. *Nat Methods* 15: 379 – 386

Hirabayashi Y, Gotoh Y (2010) Epigenetic control of neural precursor cell fate during development. *Nat Rev Neurosci* 11: 377 – 388

Huang JY, Krebs BB, Miskus ML, Russell ML, Duffy EP, Graf JM, Lu HC (2020) Enhanced FGFR3 activity in postmitotic principal neurons during brain development results in cortical dysplasia and axonal tract abnormality. *Sci Rep* 10: 18508

Johnson MR, Shkura K, Langley SR, Delahaye-Duriez A, Srivastava P, Hill WD, Rackham OJ, Davies G, Harris SE, Moreno-Moral A *et al* (2016) Systems genetics identifies a convergent gene network for cognition and neurodevelopmental disease. *Nat Neurosci* 19: 223 – 232

Journiac N, Gilabert-Juan J, Cipriani S, Benit P, Liu XQ, Jacquier S, Faivre V, Delahaye-Duriez A, Csaba Z, Hourcade T *et al* (2020) Cell metabolic alterations due to Mcph1 mutation in microcephaly. *Cell Rep* 31: 107506

Kalebic N, Taverna E, Tavano S, Wong FK, Suchold D, Winkler S, Huttner WB, Sarov M (2016) CRISPR/Cas9-induced disruption of gene expression in mouse embryonic brain and single neural stem cells in vivo. *EMBO Rep* 17: 338 – 348

Kalebic N, Gilardi C, Stepien B, Wilsch-Brauninger M, Long KR, Namba T, Florio M, Langen B, Lombardot B, Shevchenko A *et al* (2019) Neocortical expansion due to increased proliferation of basal progenitors is linked to changes in their morphology. *Cell Stem Cell* 24: 535 – 550

Kawauchi T, Shikanai M, Kosodo Y (2013) Extra-cell cycle regulatory functions of cyclin-dependent kinases (CDK) and CDK inhibitor proteins contribute to brain development and neurological disorders. *Genes Cells* 18: 176 – 194

Kosodo Y, Roper K, Haubensak W, Marzesco AM, Corbeil D, Huttner WB (2004) Asymmetric distribution of the apical plasma membrane during neurogenic divisions of mammalian neuroepithelial cells. *EMBO J* 23: 2314 – 2324

Krall AS, Xu S, Graeber TG, Braas D, Christofk HR (2016) Asparagine promotes cancer cell proliferation through use as an amino acid exchange factor. *Nat Commun* 7: 11457

Krall AS, Mullen PJ, Surjono F, Momcilovic M, Schmid EW, Halbrook CJ, Thambundit A, Mittelman SD, Lyssiotis CA, Shackelford DB *et al* (2021) Asparagine couples mitochondrial respiration to ATF4 activity and tumor growth. *Cell Metab* 33: 1013 – 1026

La Manno G, Soldatov R, Zeisel A, Braun E, Hochgerner H, Petukhov V, Lidschreiber K, Kastriti ME, Lonnerberg P, Furlan A *et al* (2018) RNA velocity of single cells. *Nature* 560: 494 – 498

Lange C, Garcia MT, Decimo I, Bifari F, Eelen G, Quaegebeur A, Boon R, Zhao H, Boeckx B, Chang JL *et al* (2016) Relief of hypoxia by angiogenesis promotes neural stem cell differentiation by targeting glycolysis. *EMBO J* 35: 924 – 941

Li H, Durbin R (2009) Fast and accurate short read alignment with burrows-wheeler transform. *Bioinformatics* 25: 1754 – 1760

Lomelino CL, Andring JT, McKenna R, Kilberg MS (2017) Asparagine synthetase: function, structure, and role in disease. *J Biol Chem* 292: 19952 – 19958

LoTurco JJ, Owens DF, Heath MJ, Davis MB, Kriegstein AR (1995) GABA and glutamate depolarize cortical progenitor cells and inhibit DNA synthesis. *Neuron* 15: 1287 – 1298

Mastrototaro G, Zaghi M, Sessa A (2017) Epigenetic Mistakes in Neurodevelopmental Disorders. *J Mol Neurosci* 61: 590 – 602

Mazur-Kolecka B, Frackowiak J (2006) Neprilysin protects human neuronal progenitor cells against impaired development caused by amyloid-beta peptide. *Brain Res* 1124: 10 – 18

McCarthy DJ, Campbell KR, Lun AT, Wills QF (2017) Scater: pre-processing, quality control, normalization and visualization of single-cell RNA-seq data in R. *Bioinformatics* 33: 1179 – 1186

Molyneaux BJ, Arlotta P, Menezes JRL, Macklis JD (2007) Neuronal subtype specification in the cerebral cortex. *Nat Rev Neurosci* 8: 427 – 437

Naka H, Nakamura S, Shimazaki T, Okano H (2008) Requirement for COUP-TFI and II in the temporal specification of neural stem cells in CNS development. *Nat Neurosci* 11: 1014 – 1023

Namba T, Dóczi J, Pinson A, Xing L, Kalebic N, Wilsch-Bräuninger M, Long KR, Vaid S, Lauer J, Bogdanova A *et al* (2020) Human-specific ARHGAP11B acts in mitochondria to expand neocortical progenitors by Glutaminolysis. *Neuron* 105: 867 – 881

Nassa G, Salvati A, Tarallo R, Gigantino V, Alexandrova E, Memoli D, Sellitto A, Rizzo F, Malanga D, Mirante T *et al* (2019) Inhibition of histone methyltransferase DOT1L silences ERalpha gene and blocks proliferation of antiestrogen-resistant breast cancer cells. *Sci Adv* 5: eaav5590

Okada Y, Feng Q, Lin Y, Jiang Q, Li Y, Coffield VM, Su L, Xu G, Zhang Y (2005) hDOT1L links histone methylation to Leukemogenesis. *Cell* 121: 167 – 178

Palozola KC, Donahue G, Liu H, Grant GR, Becker JS, Cote A, Yu H, Raj A, Zaret KS (2017) Mitotic transcription and waves of gene reactivation during mitotic exit. *Science* 358: 119 – 122

Pereira JD, Sansom SN, Smith J, Dobenecker M-W, Tarakhovsky A, Livesey FJ (2010) Ezh2, the histone methyltransferase of PRC2, regulates the balance between self-renewal and differentiation in the cerebral cortex. *Proc Natl Acad Sci U S A* 107: 15957 – 15962

Roidl D, Hellbach N, Bovio PP, Villarreal A, Heidrich S, Nestel S, Grüning BA, Boenisch U, Vogel T (2016) DOT1L activity promotes proliferation and protects cortical neural stem cells from activation of ATF4-DDIT3-mediated ER stress In vitro. *Stem Cells* 34: 233 – 245

Roubinet C, White IJ, Baum B (2021) Asymmetric nuclear division in neural stem cells generates sibling nuclei that differ in size, envelope composition, and chromatin organization. *Curr Biol* 31: 3973 – 3983

Ruzzo EK, Capo-Chichi J-M, Ben-Zeev B, Chitayat D, Mao H, Pappas AL, Hitomi Y, Lu Y-F, Yao X, Hamdan FF *et al* (2013) Deficiency of asparagine synthetase causes congenital microcephaly and a progressive form of encephalopathy. *Neuron* 80: 429 – 441

Sagar S, Hermann JS, Pospisilik JA (2018) High-throughput single-cell RNA sequencing and data analaysis. *Methods Mol Biol* 1766: 257 – 283

Schenk J, Wilsch-Bräuninger M, Calegari F, Huttner WB (2009) Myosin II is required for interkinetic nuclear migration of neural progenitors. *Proc Natl Acad Sci U S A* 106: 16487 – 16492

Schindelin J, Arganda-Carreras I, Frise E, Kaynig V, Longair M, Pietzsch T, Preibisch S, Rueden C, Saalfeld S, Schmid B *et al* (2012) Fiji: an open-source platform for biological-image analysis. *Nat Methods* 9: 676 – 682

Schleinitz D, Seidel A, Stassart R, Klammt J, Hirrlinger PG, Winkler U, Kohler S, Heiker JT, Schonauer R, Bialek J *et al* (2018) Novel mutations in the asparagine synthetase gene (ASNS) associated with microcephaly. *Front Genet* 9: 245

Shiratori R, Furuichi K, Yamaguchi M, Miyazaki N, Aoki H, Chibana H, Ito K, Aoki S (2019) Glycolytic suppression dramatically changes the intracellular metabolic profile of multiple cancer cell lines in a mitochondrial metabolism-dependent manner. *Sci Rep* 9: 18699 – 18615

Shull G, Haffner C, Huttner WB, Kodandaramaiah SB, Taverna E (2019) Robotic platform for microinjection into single cells in brain tissue. *EMBO Rep* 20: e47880

Shull G, Haffner C, Huttner WB, Taverna E, Kodandaramaiah SB (2021) Manipulation of single neural stem cells and neurons in brain slices using robotic microinjection. *J Vis Exp* 167: 61599

Street K, Risso D, Fletcher RB, Das D, Ngai J, Yosef N, Purdom E, Dudoit S (2018) Slingshot: cell lineage and pseudotime inference for single-cell transcriptomics. *BMC Genomics* 19: 477

Stuart T, Butler A, Hoffman P, Hafemeister C, Papalexi E, Mauck WM 3rd, Hao Y, Stoeckius M, Smibert P, Satija R (2019) Comprehensive integration of single-cell data. *Cell* 177: 1888 – 1902

Tavano S, Taverna E, Kalebic N, Haffner C, Namba T, Dahl A, Wilsch-Brauninger M, Paridaen JTML, Huttner WB (2018) Insm1 induces neural progenitor delamination in developing neocortex via downregulation of the Adherens Junction Belt-specific protein Plekha7. *Neuron* 97: 1299

Taverna E, Haffner C, Pepperkok R, Huttner WB (2012) A new approach to manipulate the fate of single neural stem cells in tissue. *Nat Neurosci* 15: 329 – 337

Taverna E, Götz M, Huttner WB (2014) The cell biology of neurogenesis: toward an understanding of the development and evolution of the neocortex. *Annu Rev Cell Dev Biol* 30: 465 – 502

Telley L, Agirman G, Prados J, Amberg N, Fievre S, Oberst P, Bartolini G, Vitali I, Cadilhac C, Hippenmeyer S *et al* (2019) Temporal patterning of apical progenitors and their daughter neurons in the developing neocortex. *Science* 364: eaav2522

Teratani-Ota Y, Yamamizu K, Piao Y, Sharova L, Amano M, Yu H, Schlessinger D, Ko MS, Sharov AA (2016) Induction of specific neuron types by overexpression of single transcription factors. *In Vitro Cell Dev Biol Anim* 52: 961 – 973

Vatapalli R, Sagar V, Rodriguez Y, Zhao JC, Unno K, Pamarthy S, Lysy B, Anker J, Han H, Yoo YA *et al* (2020) Histone methyltransferase DOT1L coordinates AR and MYC stability in prostate cancer. *Nat Commun* 11: 4153

Vlaming H, McLean CM, Korthout T, Alemdehy MF, Hendriks S, Lancini C, Palit S, Klarenbeek S, Kwesi-Maliepaard EM, Molenaar TM *et al* (2019) Conserved crosstalk between histone deacetylation and H3K79 methylation generates DOT1L-dose dependency in HDAC1-deficient thymic lymphoma. *EMBO J* 38: e101564

Wilsch-Brauninger M, Peters J, Paridaen JTML, Huttner WB (2012) Basolateral rather than apical primary cilia on neuroepithelial cells committed to delamination. *Development* 139: 95 – 105

Wong FK, Haffner C, Huttner WB, Taverna E (2014) Microinjection of membrane-impermeable molecules into single neural stem cells in brain tissue. *Nat Protoc* 9: 1170 – 1182

Wooten M, Ranjan R, Chen X (2020) Asymmetric histone inheritance in asymmetrically dividing stem cells. *Trends Genet* 36: 30 – 43

Zheng X, Boyer L, Jin M, Mertens J, Kim Y, Ma L, Ma L, Hamm M, Gage FH, Hunter T (2016) Metabolic reprogramming during neuronal differentiation from aerobic glycolysis to neuronal oxidative phosphorylation. *Elife* 5: e13374